The present work was submitted to:

RWTH Aachen University
Institute for industrial furnaces and heat engineering

Thermographic measurements on high temperature solar absorber coatings under concentrated solar flux

MASTER'S THESIS

Presented by:	Nils Prante Student ID: 311148
1st examiner:	Univ.-Prof. Dr.-Ing Herbert Pfeifer
2nd examiner:	Dr.-Ing. Thomas Echterhof
Date of submission:	October 1st, 2018

In cooperation with:

German Aerospace Center (DLR)
Institute of Solar Research
Plataforma Solar de Almería, Tabernas (Spain)

The present examination was prepared at the Institute for industrial furnaces and heat engineering (IOB) of the RWTH Aachen University in cooperation with the German Aerospace Center (DLR).

RWTH Aachen
Institute for industrial furnaces and heat engineering (IOB)
Kopernikusstr. 10
52074 Aachen, Germany
Phone : +49 (0) 241-80 25935
E-Mail: contact@iob.rwth-aachen.de

German Aerospace Center (DLR)
Institute of Solar Research
Paseo de Almería, 73 - 2
04001 Almeria, Spain
Phone : +49 (0) 220 360 14 223

Supervisor: Dipl.-Ing. Simon Caron
Institute of Solar Research, German Aerospace Center

1st examiner: Univ.-Prof. Dr.-Ing Herbert Pfeifer
Institute for industrial furnaces and heat engineering, RWTH Aachen University

2nd examiner: Dr.-Ing. Thomas Echterhof
Institute for industrial furnaces and heat engineering, RWTH Aachen University

Declaration of academic honesty / Eidesstattliche Erkärung

I hereby declare to have written the present master's thesis on my own, having used no other resources and tools than the listed. All contents cited from published or nonpublished documents are indicated as such.

Hiermit erkläre ich, dass ich die vorliegende Masterarbeit selbständig verfasst und keine anderen als die angegebenen Hilfsmittel verwendet habe. Alle Inhalte, die wörtlich oder sinngemäß aus veröffentlichten oder nicht veröffentlichten Schriften entnommen sind, sind als solche kenntlich gemacht.

City, Date
Ort, Datum

Signature
Unterschrift

Abstract

In the course of the Raiselife project, three uncoated and twelve black coated tubular solar receiver samples are investigated in an accelerated ageing test campaign to evaluate their durability . Thermal cycling tests are carried out, in which sample surfaces are exposed to concentrated solar flux at a modified solar dish system located at PSA in the south of Spain. Sample surface temperature needs to be controlled during cycling tests to be maintained below a maximum temperature setpoint, characterize possible degradation mechanisms and improve knowledge about the thermal cycling test procedure.

Two approaches for surface temperature measurement are applied. The existing temperature measurement system consisting of thermocouples and a tool to estimate the temperature gradient between the embedded thermocouple and sample surface. This method is enhanced by a simulation using ANSYS Thermal, confirming its applicability. A second temperature measurement system consisting of a solar blind IR camera is implemented. After confirming its calibration and applicability under the desired circumstances, an IR image is taken during cycling. Measured raw values of sample surface temperature are weighted with their specific thermal emittance in the wavelength range of the camera.

Coated samples show stable thermal emittance values throughout cycling tests. Uncoated samples show optical degradation influencing the outcome of IR image processing, allowing the applicability of precise thermographic measurements to only be ensured for coated samples. A refinement of ANSYS Thermal properties promises more reliable simulation results. An improvement on the optical characterization process of sample surfaces promises more reliable thermographic measurements, in order to decrease its sensitivity with respect to emittance.

Kurzfassung

Im Rahmen des Raiselife Projekts werden drei unbeschichtete und zwölf schwarz beschichtete Rohrproben für Solarreceiver in einer beschleunigten Alterungstestkampagne hinsichtlich Beständigkeit untersucht. Zyklische Tests, bei denen Probenoberflächen einem konzentrierten solaren Strahlungsfluss ausgesetzt sind, werden in einer modifizierten Dish-Anlage auf der PSA in Südspanien durchgeführt. Die Temperatur der Probenoberfläche muss während der Tests jederzeit bekannt sein um einen Temperatursollwert einzuhalten, mögliche Degradationsmechanismen zu charakterisieren und das Wissen über die Zyklusroutine zu verbessern.

Zwei Ansätze zur Oberflächentemperaturmessung werden angewendet. Das bestehende Temperaturmesssystem aus Thermoelementen und einer Berechnung zur Ableitung des Temperaturgradienten zwischen dem eingebetteten Thermoelement und der Probenoberfläche wird durch eine Simulation mit *ANSYS Thermal* erweitert, wodurch die Anwendbarkeit der zuvor eingesetzten Methode bestätigt wird. Ein zweites Temperaturmesssystem, bestehend aus einer solarblinden IR-Kamera wird implementiert. Nach Bestätigung der korrekten Kamerakalibrierung und der Anwendbarkeit unter den gewünschten Umständen wird ein IR-Bild aufgenommen. Gemessene Rohwerte der Oberflächentemperatur werden mit dem spezifischen thermischen Emissionsgrad der jeweiligen Probe im Wellenlängenbereich der Kamera gewichtet.

Beschichtete Proben zeigen während der zyklischen Tests stabile thermische Emissionsgrade. Unbeschichtete Proben zeigen eine optische Degradierung, die das Ergebnis der Infrarotbildverarbeitung beeinflusst. Dadurch kann die Anwendbarkeit präziser thermografischer Messungen nur für beschichtete Proben mit stabilem Emissionsgrad sichergestellt werden. Durch eine Verfeinerung der *ANSYS* Simulation werden zuverlässigere Ergebnisse erwartet. Eine Verbesserung des optischen Charakterisierungsprozesses von Probenoberflächen verspricht zuverlässigere thermographische Messungen aufgrund der nachgewiesenen Empfindlichkeit gegenüber des Emissionsgrades.

Table of Contents

List of symbols and units

Symbol	Meaning	Unit
η	Efficiency	-
α	Absorptance	-
ε	Emittance	-
τ	Transmittance	-
ρ, R	Reflectance	-
λ	Wavelength | Heat conduction coefficient	nm or µm | W/m·K
E	Irradiance	W/m²
ϕ,Q	Radiant Flux	W/m²
ν	Frequency	Hz
Ω	Solid angle	sr
T	Temperature	°C
A	Area	m²
G	Spectrum for solar direct normal irradiance	W/m²·nm
F	View factor	-

Index	Meaning
sol	Solar
th	Thermal
abs	Absolute
g	Gain
l	Loss
rad	Radiation
conv	Convection
ext	External
int	Internal
f	Fluid
amb	Ambient
BB	Blackbody
max	Maximum
atm	Atmosphere
det	Detector
r	Reference
s	Sample

List of constants

Symbol	Name	Value	Unit	Source
k	Boltzmann constant	$1.381 \cdot 10^{-23}$	J/K	[1]
σ	Stefan-Boltzmann constant	$5.670 \cdot 10^{-8}$	$W/m^2 \cdot K^{-4}$	[1]
h	Planck constant	$6.626 \cdot 10^{-34}$	$J \cdot s$	[1]
c_0	Speed of light in vacuum	$299{,}792{,}458$	m/s	[1]
-	Solar constant	1361	W/m^2	[2]

List of Abbreviations

Abbreviation	Meaning
DLR	German Aerospace Center/ Deutsches Zentrum für Luft- und Raumfahrt
IOB	Institute for industrial furnaces and heat engineering/ Institut für Industrieofenbau und Wärmetechnik
RWTH	Rheinisch-Westfälische Technische Hochschule Aachen
PV	Photovoltaics
LCOE	Levelized Cost of Energy
LCOC	Levelized Costs of Coating
CSP	Concentrated Solar Power
EU	European Union
Raiselife	Raising the Lifetime of Functional Materials for Concentrated Solar Power Technology [3]
CIEMAT	Center for Energy, Environment and Technology Research/ Centro de Investigaciones Energéticas, Medioambientales y Tecnológicas
PSA	Plataforma Solar de Almería
DNI	Direct Normal Irradiation
PTC	Parabolic Trough Collector
(N) IR	(Near-) Infrared
FTIR	Fourier Transform Infrared
TMS	Temperature Measurement System
(U) FPA	(Uncooled) Focal Plane Array
FOV	Field of view
NBP	Narrow Band Pass
AM	Air Mass
OD	Outer diameter
3D	Three-dimensional
FWHM	Full Width at Half Maximum

Abbreviation	Meaning
VIS	Visible spectrum
UV	Ultraviolet
SW	Short-wave
MW	Mid-wave
LW	Longwave

1. Introduction

The world´s energy demand is rising quickly. Newly industrialized countries entering global markets, the implementation of emerging technologies and a continuous growth in digitalization and information technology are only a few of the various reasons. In 2017 the world´s total consumption of energy increased by $2.3\,\%$ in only one year, which means that it more than doubled in comparison to the previous year ($1{,}1\,\%$ in 2016) [4].

On the other hand, global warming and human impact on nature is becoming more crucial than ever. To reach the agreed goal of Paris Climate Convention in 2015, the rise of global average temperature must remain below $2\,°C$ compared to the pre-industrial era [5]. Therefore, constant development and strategic combination of renewable energy applications throughout the world is imperative. However, for new technologies to be established in an economically meaningful way, the financial aspect has to be considered as well. Photovoltaics (PV) and wind systems show favorable energy generation prices but a low capacity factor due to their unavailability on demand. On the other hand, the implementation of an electrical energy storage system to solve this problem would yet significantly increase capital costs. Considering the Levelized Cost of Energy (LCOE), renewables show a great potential compared to conventional energy sources, which yet has to be leveraged entirely. The LCOE of conventional energy sources such as coal remained rather constant at 100 to $110\,\$/MWh$ during the last decade while the LCOE of nuclear energy increased from $96\,\$/MWh$ in 2010 to $148\,\$/MWh$ in 2017. A decrease in LCOE, especially for PV and wind energy, made renewables cost-competitive to conventional power generation technologies [6]. The execution of a large-scale Concentrated solar power (CSP) project even promises to achieve an LCOE of $73\,\$/MWh$ [7] which lowers the costs by up to $60\,\%$ compared to existing CSP systems (98 to $181\,\$/MWh$) [6].

The aim of the European Union (EU) is to achieve a reduction of greenhouse gas emissions by $40\,\%$ compared to 1990 levels and a $27\,\%$ share for renewable energy until 2030 [5]. Through research projects such as *Raiselife*, which is part of the *Horizon 2020* program, the EU-wide achievement of the aforementioned goals is implemented in politics and science. This project focuses on raising the lifetime of key functional materials that determine the LCOE for CSP technologies significantly. A consortium of industry leaders, small and medium-sized enterprises and research institutes of the concentrated solar thermal and materials sector has been created to rapidly establish advances from several working groups in CSP industry applications. The focus of the various working groups lies on reflector and concentrator improvement, degradation and corrosion resistance research as well as on economic implementation [3].

This thesis is part of the third working package of the Raiselife Project, with main emphasis on CSP receiver coatings. It is carried out at the joint investigation site of the *German Aerospace Centre* (Deutsches Zentrum für Luft- und Raumfahrt, DLR) and the Spanish *Centre for energy, environmental and technological investigation* (Centro de Investigaciones Energéticas, Medioambientales y Tecnológicas, CIEMAT) in Tabernas, Spain (See Figure 1).

Figure 1: Aerial Image of the *Plataforma Solar de Almería (PSA)* in Tabernas, Spain [8]

Different solar receiver sample tubes made out of high temperature metal alloys and coated with various types of absorber coatings are tested at high temperature to investigate their durability. Therefore an accelerated ageing test campaign is carried out to evaluate the long-term behavior under cyclic concentrated solar flux. The goal of this thesis is to improve the temperature measurement system during the test campaign to create a deeper understanding of the temperatures that are present on the surface of the coated samples.

In the scope of this thesis, the existing temperature measurement system (TMS) is extended by a thermal simulation to properly take into account thermal influences. Additionally another TMS is implemented. A thermal imaging camera is calibrated in the laboratory and mounted at the test bench. A thermal image of the hot sample surface is created after various steps of camera calibration. At the end, both TMS are compared and the deviation of the resulting temperature is examined.

2. Background

The following chapter is intended to give a general overview of the different concepts in CSP technology. On the basis of linear concentrating and point concentrating systems, different technologies are distinguished. Thereafter, the state of the art in the development of solar absorber coatings is considered. At the end of the chapter, an insight into the current technology of temperature measurement on receiver surfaces is given. Subsequently, the test bench on which the experiments have been carried out in the context of this thesis is explained.

2.1 CSP Plants

The utilization of concentrated solar energy has a long past in the history of mankind. Ancient populations of Greece and China already created fire with mirrors and glasses. Fueled by the progress of industrialization, the human hunger for energy reached new spheres from the middle of the 19th century onwards. It has been satisfied by conventional power plants over decades [9]. An exception could probably be the effort of erecting a parabolic trough collector in 1913. A $45\ kW$ steam engine powered by solar radiation was used to pump water from Nile River for agricultural use in Al Meadi, Egypt [10]. Rethinking did not start until the 1970s, when the rising perception of global warming and the recent oil crises made alternative and environmentally friendly energy sources necessary [11]. As a result, intensive reseach and development efforts have been initiated and first commercial solar power plants were erected in the 1980s.

Nowadays several different technologies for energy generation from solar radiation can be applied. The world's most widely used solar power generation technology is PV, by which incident photons are directly converted into electrical energy [9]. In CSP technology on the other hand, the incident solar radiation is first concentrated, which initially generates heat. In a second step, the generated heat is converted into electricity by a steam or a gas turbine. This two-step method has the great advantage, that the generated heat can also be stored and converted into electricity at a later point in time. As a result, CSP has the potential to compete with existing baseload power plants because of the greater availability compared to PV or wind energy. Furthermore a combination of conventional and CSP power plant types is conceivable and has been implemented at Hassi R'Mal Power Plant in Algeria where the solar heat partially substitutes the fossil natural gas fuel [12].

A common feature of all CSP technologies is that only direct solar irradiation can be focused and transformed into heat. In order to reach a sufficient operating temperature and hence, to conduct a CSP power plant economically, Direct Normal Irradiation (DNI) has to be at a level above $2000\ kWh/m^2$ per year [9]. Figure 2 shows the average worldwide and daily DNI. It can be stated that North and South Africa, Australia, central parts of South and North America, and the Middle East show excellent conditions for the application of CSP. Also adjacent regions exhibit a DNI-Level of above $2000\ kWh/m^2$ per year, whereupon northern parts of Europe, North and Latin America as well as central parts of Africa and East Asia seem to be rather unsuitable.

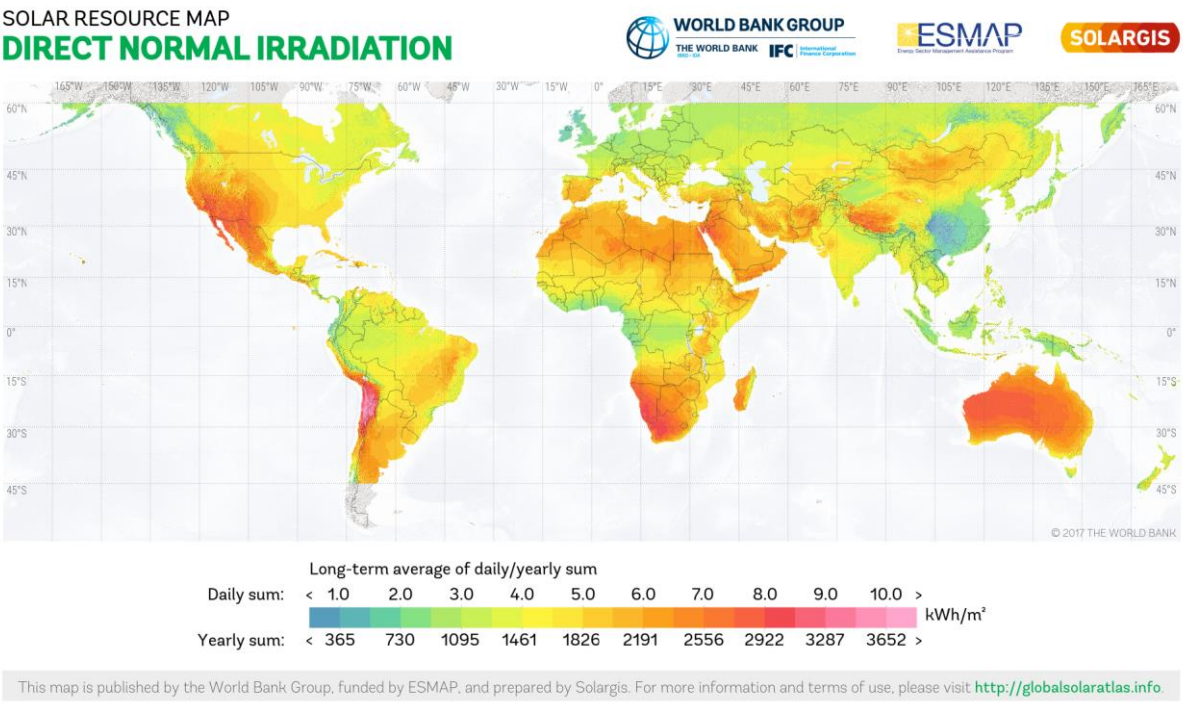

Figure 2: Average worldwide annual and daily DNI in kWh/m² [13]

A difference between CSP technologies is the way of concentrating the incident solar radiation. A distinction is made between line and point concentrating systems, which is explained in more details below.

2.1.1 Line concentrating systems

The most widely applied type of all power plant designs for generating energy using concentrated solar radiation is a line-focusing system design. Until the last decade, Parabolic trough systems have been the only long-term commercially proven technology to use solar energy in large power plants [14].

Parabolic trough collectors:

In Parabolic trough collector (PTC) power plants, parabolic shaped mirrors are aligned along an axis forming a longitudinal trough. The incident solar radiation is concentrated on receiver tubes at the focal line of the parabolic shape. Enclosed in an evacuated glass envelope, one receiver tube is usually coated with a selective absorber paint ensuring a high level of solar absorptance and a low level of thermal emittance. Conventional and selective paintings for solar absorbers are explained more precisely in the following chapter. A heat transfer fluid flowing inside the tube is either used for creating steam or directly fueling a turbine in a following step [15]. To exploit the highest possible level of solar irradiation, parabolic trough collectors are equipped with a one-axis tracking system allowing the unit to follow the path of the sun during the day. In most commercial applications, north-south orientated collectors are predominant. The reason is a higher annual average

yield that can be obtained using this alignment, whereas east-west orientated collectors provide a better testing set up during solar noon [16].

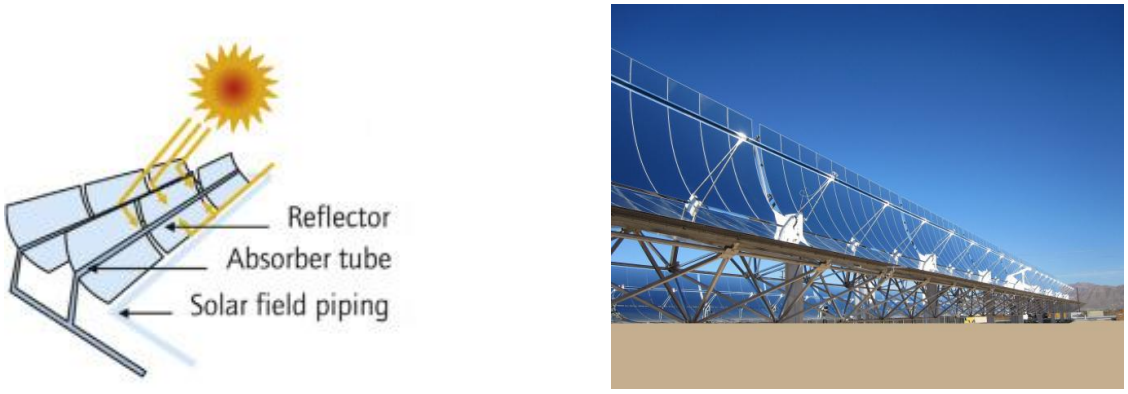

Figure 3: Working scheme of a Parabolic Trough collector (left) and image of a PTC power plant in operation (right) [17, 18]

Linear Fresnel collectors:

Linear Fresnel collector systems consist of long but narrow mirror rows. Every single row is rotatable along its longitudinal axis allowing the sunlight to be reflected and concentrated along a stationary receiver line above the mirror rows. The receiver consists of an absorber tube in a downwardly open housing, in which there may also be another focusing apparatus located (a so-called second stage concentrator) to harness most of the incoming radiation. The fluid used in most commercial applications to transfer the heat is water which is being evaporated and superheated. Subsequently it is used to fuel a steam turbine to produce electricity. Linear Fresnel collectors are erected with a high share of standard construction components, enabling a large number of local added value [14]. In addition, wind loads can be diminished through the plane arrangement of the mirrors in a superior way compared to parabolic trough collectors [19]. On the other hand, cosine losses, blocking and shading lower the overall optical efficiency of a Linear Fresnel setup [20].

Figure 4: Working scheme of a Linear Fresnel collector (left) and image of a Linear Fresnel power plant in operation (right) [18, 21]

2.1.2 Point concentrating systems

The concentration levels of solar irradiation for line concentrating systems are usually below 100, whereas with the deployment of point concentrating systems levels of around 600 (solar tower) or even above 1000 (parabolic dish) are feasible [22]. Therefore, temperatures of up to $1200\,°C$ can be achieved at the absorber due to the higher solar flux [16].

Solar Tower Systems:

Solar Tower systems consist of up to several thousands of tiltable mirrors (so-called heliostats) and a receiver that is mounted on a tower at a central position of the mirror field. A two-axis tracking system at each plane or slightly concave curved mirror of the heliostat serves to trace the motion of the moving sun throughout the day and to focus its irradiation upon the surface of the receiver. Due to the high temperature, steam or molten salt is used to transfer the heat to the turbine unit of the construction, where the electricity is generated. Nowadays even attempts with liquid metal as a heat transfer medium are being carried out [23]. The arrangement of the heliostat field is highly dependent on the receiver design and on the geographical coordinates (latitude) of the whole power plant. Fields of concentric, $360\,°$ circles of heliostats that surround the receiver tower (see Figure 5,right) are just as feasible as an arrangement of heliostats in a $180\,°$ area northwards of the receiver tower (north field, see Figure 1).

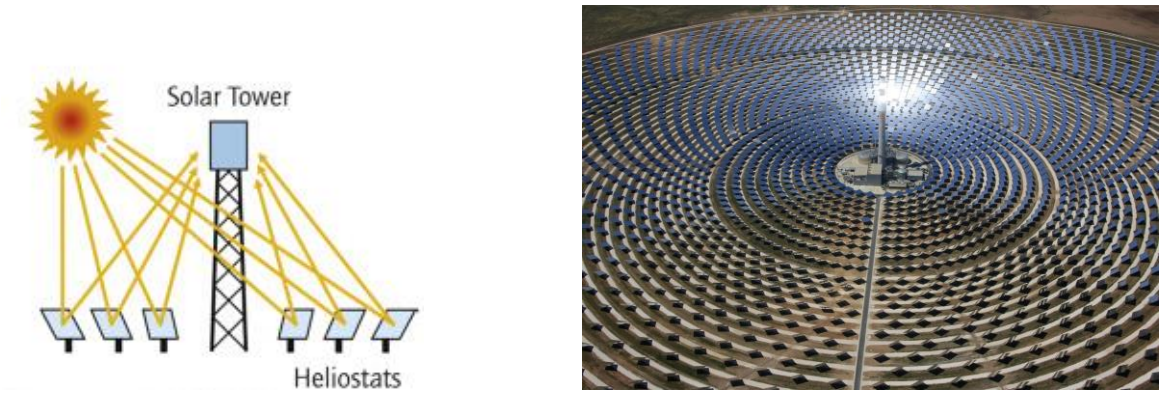

Figure 5: Working scheme of a Solar Tower system (left) and image of a Solar Tower power plant in operation (right) [18, 24]

Dish Systems:

Dish systems consist of a rotationally symmetric, parabolic shaped mirror to concentrate the solar irradiation at a focal point at the center of the construction. Due to the fact that only direct irradiation can be concentrated, a two-axis sun-tracking system that turns and elevates the whole structure has to be applied. An elevated temperature range is present at the focal point owing to the high concentration factor. The resulting heat is either dissipated by warmed-up tubes containing a heat transfer fluid or directly converted into electricity. The latter is achieved by using a downstream Stirling engine by first converting the thermal energy into mechanical energy and retrieving electricity from a generator that is connected to the Stirling engine thereafter.

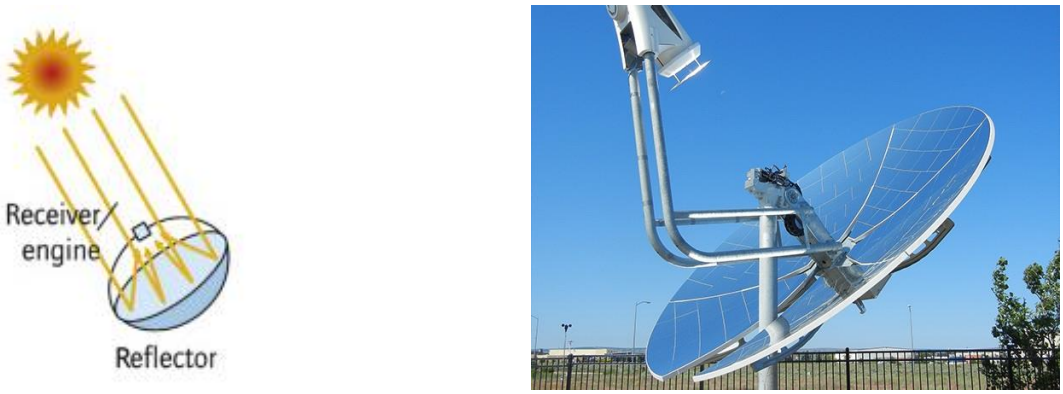

Figure 6: Working scheme of a Solar Dish system (left) and image of a Solar Dish facility in operation (right) [18, 25]

2.2 Solar Absorber Coatings

The power cycle efficiency of Solar Tower systems can be increased with higher central receiver operating temperatures. Therefore, the energy absorbed by the receiver must be maximized and the heat loss from the receiver to the environment must be minimized. The aforementioned heat loss occurs due to radiation losses from the hot receiver surface to the environment and also due to convection from wind and buoyancy effects [23]. Hence, the efficiency of a central receiver unit and therefore the efficiency of the whole power plant is strongly dependent on the coated receiver surface behavior. Equation (1) [26] balances the absorbed solar radiation and the radiation emitted by the absorber to determine the coating's opto-thermal efficiency $\eta_{coating}$, neglecting convective losses. The incident solar radiation $Q_{sol,}$ the solar absorptance α_{sol}, the thermal emitance ε_{th}, the Stefan-Boltzmann-Constant σ and the absorber Temperature T_{abs} are taken into consideration.

$$\eta_{coating} = \frac{\alpha_{sol} \,.\, Q_{sol} - \varepsilon_{th} \,.\, \sigma \,.\, {T_{abs}}^4}{Q_{sol}} \tag{1}$$

The standard product that is used on most of previous CSP central receivers is the high temperature paint *Pyromark Series 2500* (see Appendix for more information). The advantages coming along with the deployment of this product are an easy application, a relatively high solar absorptance of 0.96 and a relatively low price. However, due to a thermal emittance of 0.87 the paint experiences large thermal losses during high temperature operation. When operated in air, it also shows significant degradation at temperatures above $700\,°C$. This results in a drop of performance and a potential increase in operating costs for CSP facilities due to the more frequent necessity of paint re-application [26]. Thus, another approach considering the Levelized Costs of Coating (LCOC) has been introduced. It is defined as: "The ratio of the total annualized coating costs to the annual thermal energy absorbed" [27]. Combining the two aforementioned approaches makes it possible to derive the requirements for a competitive absorber coating: High solar absorptance, low thermal emittance and high durability or respectively cost efficient coating exchangeability. In the following, two approaches to lower the LCOC will be highlighted: Selective absorber coatings and the curing of applied coatings with the use of solar irradiation.

Selective absorber coatings are already used in PTC and Linear Fresnel systems for several years. The advantage is a high solar absorptance and low heat losses due to a low emittance in the infrared range at operational temperature. However, there are some differences between aforementioned systems and power tower systems regarding selective coatings. The receiver temperature of tower systems is up to $200\,°C$ higher and the pipes are not protected while receiver tubes in line concentrating systems are housed inside a glass tube or a secondary receiver. Therefore, research is being conducted to identify suitable selective coatings for the use in power tower receivers. The goal is to maximize the absorptance in the wavelength range corresponding to the solar spectrum ($400 - 2500\,nm$) and to minimize thermal emittance in the infrared wavelengths ($1 - 20\,\mu m$). However, an overlap of these spectra at higher temperatures makes it a challenging task to meet the aforementioned requirements [27]. To manufacture a selective-coated receiver tube, several steps must be taken. First, the surface of the samples is polished, then different layers of the very thin selective absorber material are applied by magnetron sputtering. The bottom

layer consists of an IR-Reflector, followed by a Metal-Ceramic (so-called Cermet) layer and an Anti-Reflection Layer on the outer surface. Figure 7 shows an Image of Selective Coated Absorber tube samples which have the characteristic blue color [28]. Previous studies have shown that the application of selective coatings could have a positive impact on LCOC. Nevertheless, further research must be conducted owing to the lack of durability and high application cost. Due to a high degradation rate and corrosion occurring in a salt spray test, selective coated samples did not meet the quality requirements yet [29].

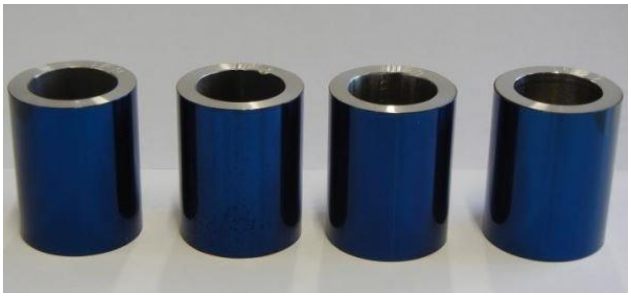

Figure 7: Image of Selective Coated absorber tube samples [28]

Not only the coating itself, but the entire process of application must be taken into account in the calculation of the LCOC. Solar absorber coatings often consist of a high-temperature-resistant paint with ceramic components. The coating is applied to the tubes of the receiver and then has to be cured for several hours at different temperatures in an oven. Under certain circumstances, it may be necessary to remove the entire receiver unit of a power tower for this process. To avoid this prohibitive expense, various solutions are considered. A novel approach is to apply the paint directly to the mounted receiver and then use the heat of the solar radiation to cure it. Initial tests show the potential but at this point, no final information on the result can be announced. However, this approach underlines that the awareness of the temperature on the surface of a solar receiver tube under concentrated solar radiation is important and necessary.

2.3 Temperature Measurement on Solar Receiver Surfaces

Surface temperatures of solar receivers are not just a criterion for process monitoring, performance and efficiency but also an important parameter for operational safety. Because local overheating quickly causes damage to individual components, a good knowledge of the thermal load of the corresponding critical parts is required. With the possible application of temperature sensors, contactless temperature measurement systems and thermal simulation, three approaches are taken into consideration.

Temperature sensors that need to contact the surface of an object under the influence of concentrated solar radiation can only be used to a limited extent, since the measurement is biased by the absorbed radiation of the sensor itself. The infrared measurement technology promises the possibility of a non-contact surface temperature measurement.

Pyrometry and thermography are nowadays widely applied in process monitoring, object recognition or, as quantitative pyrometry, also in the determination of surface temperatures. However, common IR measurement devices also have some potential measurement biases, since the concentrated solar radiation can be reflected by the measured object.. Certain adjustments need to be fulfilled in order to use contactless temperature measurements on solar absorber surfaces. Previous experiments at the PSA have been carried out regarding this issue. In summary, a possible employment of pyrometric temperature measurement in suitable atmospheric absorption bands could be confirmed to reduce solar parasitics [30, 31].

Thermal simulation is being conducted more frequently in the past years. This method is widely used and very popular because of the achievement of good results in agreement measurements. Through a more precise analysis and the consideration of dominant heat transfer sources , it has also proven itself for verifiying correct temperature measurements on solar receivers.

In the course of this thesis, different approaches for temperature measurement on solar receiver tubes under concentrated solar radiation are combined. A custom temperature sensor system is coupled with a thermal simulation to quantify the temperature difference between the coated skin and the embedded thermocouple (TMS 1). In addition, a suitable industrial IR camera is used for thermal imaging. Individual parameters such as emittance are measured for each sample in the laboratory using a FTIR spectrophotometer and directly taken into account in the measurement (TMS 2). This ensures a more accurate measurement and creates a deeper understanding of the process itself.

2.4 Solar Cycling test bench

Coatings developed within the Raiselife project are evaluated regarding performance and durability. To carry out thermal cycling tests on a set of tubular samples under concentrated solar flux, a unique test bench was constructed by DLR and CIEMAT. Combining sample temperature and solar flux control systems, it was mounted to an existing point concentrating dish apparatus with a mirror diameter of roughly $5\,m$ (see Figure 8) at the Plataforma Solar de Almería (PSA) in Tabernas, Spain.

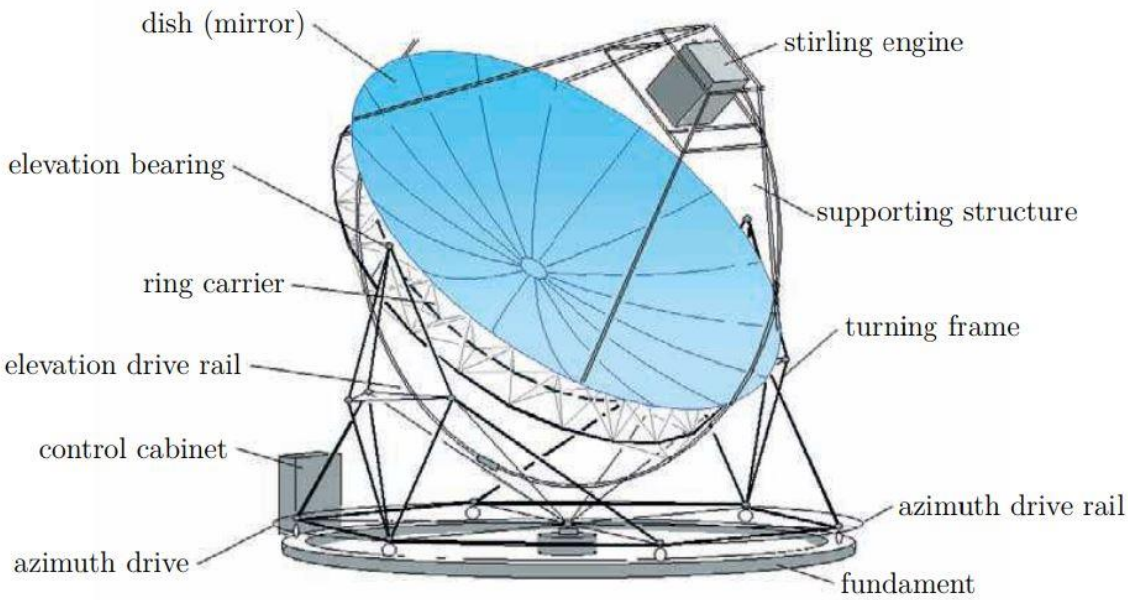

Figure 8: Main Components of a Solar Dish assembly [32]

Therefore, the Stirling engine of the Dish system is removed and replaced by the aforementioned testing unit (see Figure 9, left). Through a set of air blowers - one for each line - a dynamic temperature control is feasible for each line. A linear drive moves the samples in a perpendicular direction to the optical axis of the dish, enabling the control of the impinging solar flux Q_{sol}. Furthermore, a ceramic protection board beneath the sample lines guarantees that only the samples are irradiated by concentrated solar flux and technical equipment positioned below is protected.

Figure 9: The modified dish assembly test bench including a linear drive range, the sample tubes, a ceramic front protection and five air blowers. Long shot image (left) and close-up of the sample arrangement from the side (right) [29]

The samples are arranged in five lines with each line consisting of three samples (see Figure 9). In the current cycling test campaign, 12 black coated (four lines) and three uncoated samples (one line) are examined. The precise order of the samples is illustrated in Figure 10. Samples number 88, 89,92 and 95 are made from *Haynes230*, the rest is made from *Inconel617* substrate material. Samples number 73, 78 and 84 are uncoated, while the rest of the samples are coated with different absorber coating chemical formulations. For the exemplary presentation of experimental results, one uncoated sample (number 73) and one coated sample (number 89) have been selected (red) in the overview image. Details concerning other samples are available in the appendix section.

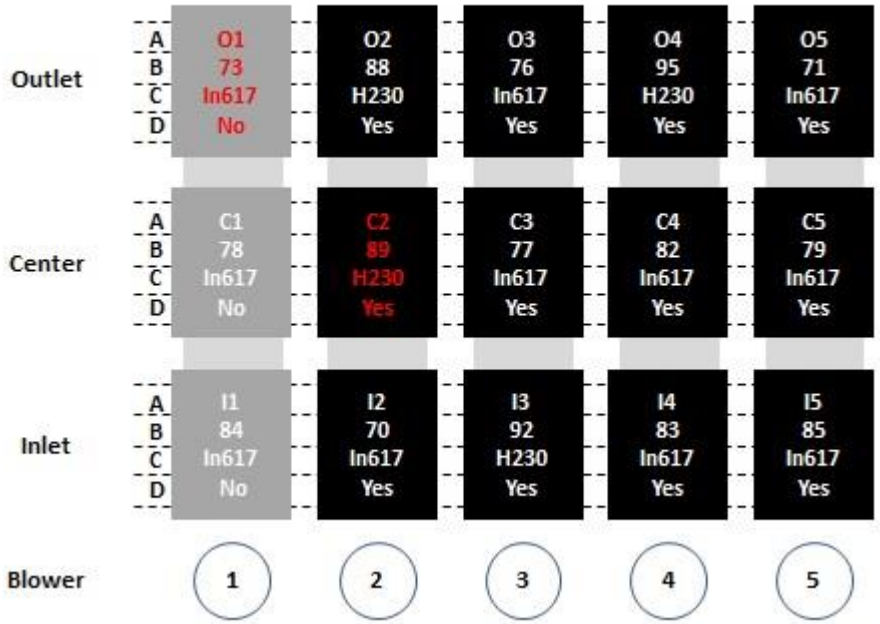

Figure 10: Overview of sample arrangement. Sample coordinates (A), sample number (B), substrate material (Inconel617 or Haynes230, C) and presence of black coating (D) is indicated. Exemplary samples are depicted in red.

To perform an accelerated ageing test campaign, the samples are exposed to thermal cycling. Each cycle consists of three sequences illustrated in Figure 11:

- ***Heating****: All probes are first heated from* 200 *to* $750\,°C$ *at a maximum heating rate of* $30\,°C/min$*. The average solar flux is gradually increased from* 40 *to* $250\,kW/m^2$*.*

- ***Dwell time****: the maximum skin temperature is then maintained at* $750\,°C$ *for* 30 *minutes. The average solar flux is maintained at* $250\,kW/m^2$ *for* 30 *minutes.*

- ***Cooling****: All probes are cooled from* 750 *to* $200\,°C$ *at a maximum cooling rate of* $-30\,°C/min$*. The average solar flux is reduced gradually from* 250 *to* $40\,kW/m^2$. [29]

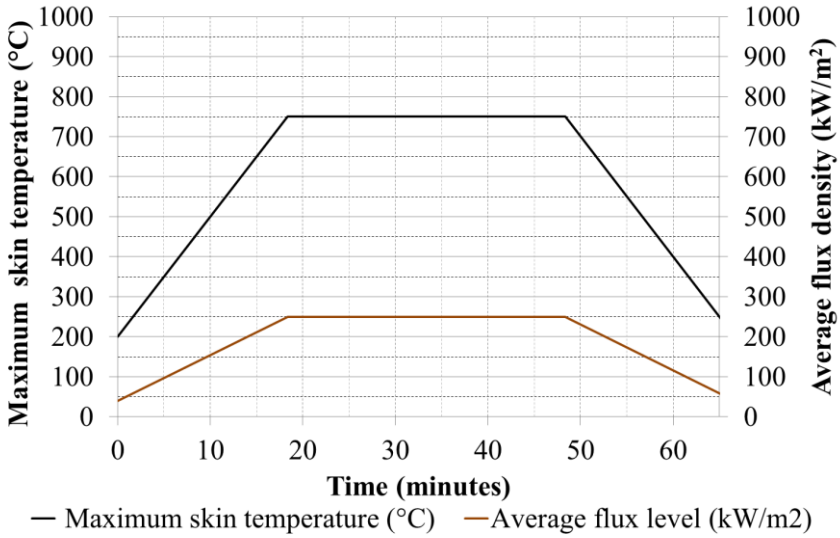

Figure 11: Temperature and flux profile of a thermal cycle [29]. With a heating rate of $30\ °C/min$ the samples are heated up from a skin temperature of $200\ °C$ to $750\ °C$. During a dwell time of 30 minutes, this maximum temperature is held constant. The cooling phase is driven symmetrically with respect to the heating phase. The development of the solar flux coincides, ranging between $40\ kW/m^2$ and $250\ kW/m^2$.

As part of the cycling routine, each sample is optically characterized before testing and after every 25 cycles. In total, 100 thermal cycles are performed in the course of one test campaign. Furthermore, microscope images are taken to identify potential degradation mechanisms, such as corrosion spots, delamination or cracks.

3. Thermocouples and gradient estimation (TMS 1)

The samples tested in the Dish test facility serve as a reference for assessing the durability of the materials used. The aim is to qualify material combinations of substrate material and coating for a possible implementation on a larger scale and for a longer period of time in the receiver of a solar tower system. In order to characterize the involved processes and to ensure that the correct temperature profile is maintained during the test, the temperature of the samples must be known at all times. The following is an insight into the existing temperature measurement system of the test bench (TMS 1). First, the assembly and the procedure for determining the surface temperature is explained. After that, a closer look is taken at the modeling approach, which is carried out to improve the temperature gradient calculation.

3.1 Fundamentals and state of the art

As already mentioned above, it is not suitable to measure the surface temperature by means of a thermocouple directly at the surface. Therefore the point of temperature measurement needs to be inside the measured structure and as close to the surface as possible. For each sample, a hole is drilled into the tubular material from the cross-sectional side. With a diameter of $1.8\,mm$ and a depth of $25\,mm$, it is placed at least $1\,mm$ below the sample skin on the irradiated side (Figure 12).

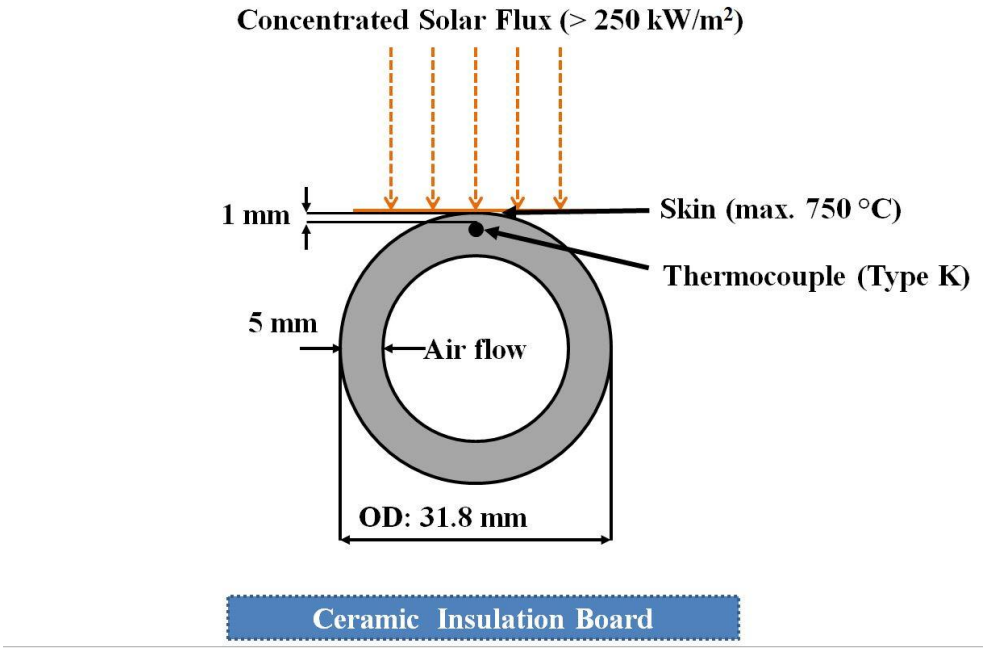

Figure 12: Cross-section of sample probe with inserted thermocouple [29]

To measure and monitor the present temperatures, Thermocouples (Type K) are inserted in the aforementioned holes, so that one line of three samples accordingly consists of three thermocouples (see Figure 13).

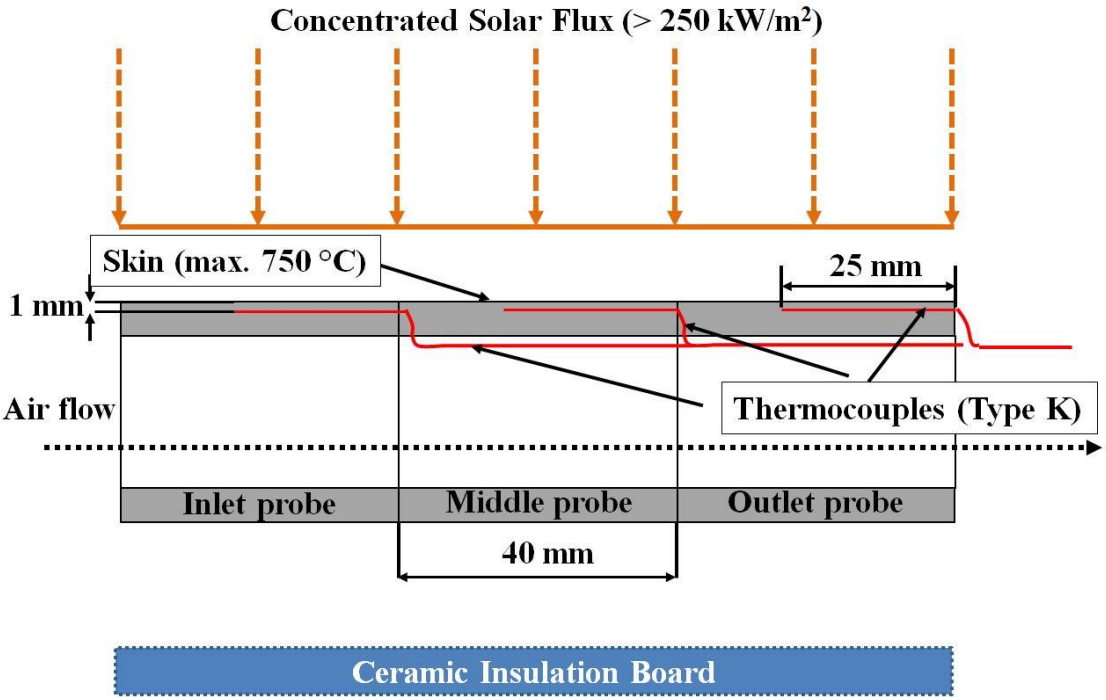

Figure 13: Longitudinal section of sample probes with inserted thermocouples [29]

However, the measured temperature at the tip of the thermocouple is not equal to the one at the surface of the sample, which requires the execution of a heat loss calculation. A simple analytical tool has been created to derive a surface temperature taking into account the respective coating thicknesses and thermal conductivities of the sample materials. It is assumed that the radiation is distributed homogeneously on one half of the sample. This tool is used to calculate heat loss for either a flat or a curved sample. Following the established routine for a targeted skin temperature of $750\,°C$, the heat loss calculated for a flat coated sample results in a value of around 30 °C with an added tolerance of $10\,°C$. Nevertheless, certain factors of heat transfer are still neglected. Radiation exchange between the samples themselves, radiation exchange between the samples and the ceramic insulation, losses due to convection and radiation emitted by the hot surface is not taken into account as well as the temperature dependence of the thermal conductivity.

3.2 Modelling Approach

To assure a more precise temperature calculation, a 3D thermal simulation is carried out. The goal is to regard the tubular geometry of the samples and the temperature dependence of the thermal conductivity coefficient λ in the calculation. Furthermore, parameters that are different for each sample are included and the simulation is performed individually for each sample in the test campaign (see Table 1). The parameters required for the simulation will be discussed in more detail below.

The strength and durability of the tube material *Inconel617* and *Haynes230* (see Appendix) do not allow highly precise machining steps under the desired circumstances. The distance between the thermocouple holes and the surface differs from sample to sample. The exact distances are therefore measured with a caliper.

As mentioned above, each sample is optically characterized before and after each 25 cycles of the test. The solar absorptance α_{sol} and the thermal emmitance ε_{th} are dependent on the surface behavior and also show variation between different samples.

To compare the results of the thermal simulation with results from thermal imaging (TMS 2) the time of the data collection plays a crucial role. The thermal imaging process which is explained in more detail below is carried out during the 12th cycle of the test. A linear interpolation between optical measurement results before and after 25 cycles provides the proper values for solar absorptance α_{Sol} and thermal emitance ε_{th} that can be used for the simulation. The cooling convection coefficient can be found via iterative variation of parameters.

The simulations are conducted using *ANSYS Thermal* (Steady-State). In a first step, important material data such as the thermal conductivity as a function of temperature is integrated. Then, a three-dimensional model of the sample geometry is created (see Figure 14 and Table 2). In the following, the heat flows occurring at the respective surfaces are applied.

Table 1: Input (1), optimization (2) and output (3) parameters of ANSYS-simulation

	Parameter	Unit	Source
1)	Thermal Emittance ε_{th}	%	Derived from reflectance measurements according to chapter 4.3
	Solar Absorptance α_{sol}	%	
	Temperature Thermocouple T_{TC}	°C	Measured during cycle test
	Distance Thermocouple from Skin	mm	Measured with caliper
	Solar Flux Q_{sol}	W/m²	Calculated according to Equation 2
	Thermal conduction substrate Material $\lambda_{substrate}$	W/m·K	Derived from Literature, see Appendix
	Thermal conduction coating $\lambda_{coating}$	W/m·K	Provided by manufacturer
2)	Cooling convection coefficient $h_{int \rightarrow f}$	W/m²·°C	Derived iteratively
3)	Skin Temperature $T_{final, TMS1}$ Interface Temperature $T_{interface}$ Inside Surface Temperature $T_{inside\ surface}$ ΔT_{ANSYS}: (Skin↔Thermocouple) ΔT: Skin↔Interface ΔT: Skin↔Inside Surface	°C	Simulation result

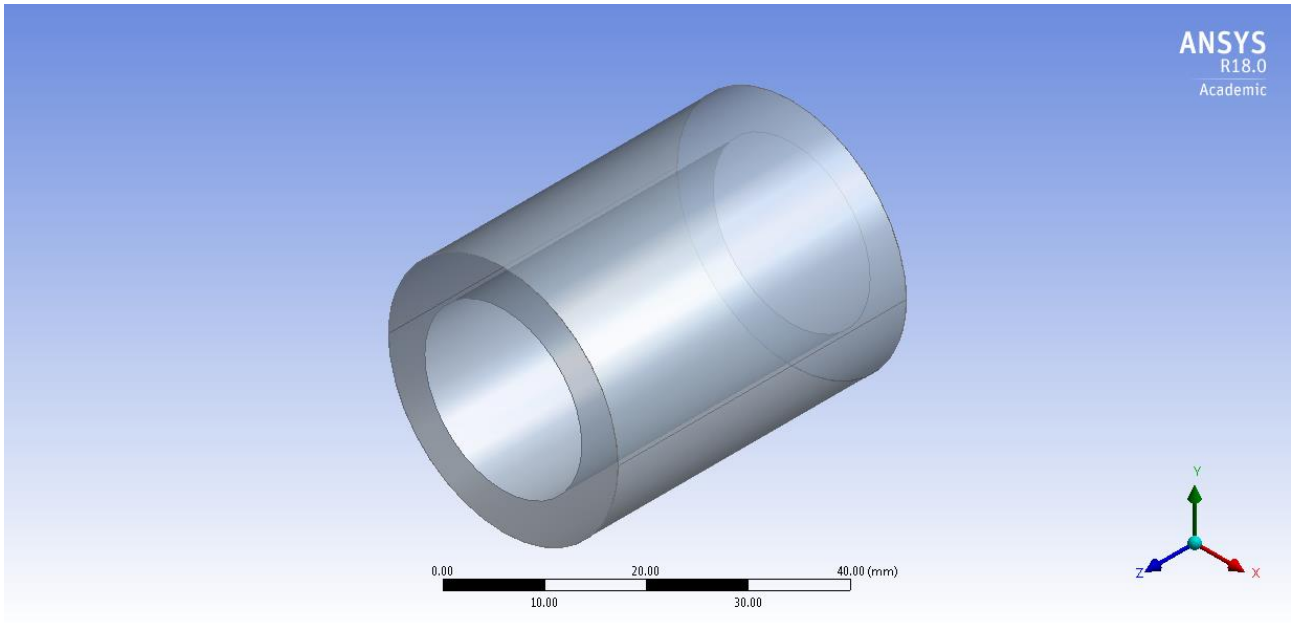

Figure 14: Three-dimensional model of the sample geometry [33]

Table 2: Common geometrical parameters of tubular samples

Parameter	**Value**
Length	40 mm
Outside diameter	31.8 mm
Inside diameter	26.8 mm
Wall thickness	5 mm
Coating thickness	0.035 mm

The heat generated by radiation on the exposed side of the samples $Q_{g,sol}$ is calculated as shown in Equation 2. The irradiated surface area A_{ext} is multiplied by the solar absorptance α_{sol} and the incident solar radiation G_{sol}.

$$Q_{g,sol} = A_{ext} \cdot \alpha_{sol} \cdot G_{sol} \tag{2}$$

The losses from the entire outer surface area to its environment due to thermal radiation $Q_{l,rad}$ is calculated as shown in Equation 3. Regarding the fact that in this case the whole hot sample is radiating, the surface area is two times the one that is irradiated by the solar heat flow. Furthermore the view factor F is set equal to one and the ambient temperature T_{amb} is set constant at $25\,°C$.

$$Q_{l,rad} = 2 \cdot A_{ext} \cdot F \cdot \sigma \cdot \varepsilon_{th} \cdot ({T_{ext}}^4 - {T_{amb}}^4) \tag{3}$$

The heat transferred to the flowing medium on the inside of the tubular geometry due to convection is calculated as shown in Equation 4. The internal surface area A_{int} is multiplied by the coefficient for convection from the internal surface to the flowing medium $h_{int\rightarrow f}$ and the difference between internal surface and flowing medium temperature $(T_{int} - T_f)$.

$$Q_{g,conv} = A_{int} \cdot h_{int\rightarrow f} \cdot (T_{int} - T_f) \tag{4}$$

More detailed information can be found in [34]. By deriving a heat balance equation with the relevant inputs and outputs, a relationship between the aforementioned equations is created to link the mentioned heat flows:

$$Q_{g,sol} = Q_{g,conv} + Q_{l,rad} \tag{5}$$

With the entered parameters, it is furthermore possible to perform a simulation that reflects the temperature distribution of the irradiated sample at each point of the sample body (see Figure 14, left). In this first simulation approach, the occurring convection from the outer sample surface to the environment and the thermal radiation on the inside of the samples are neglected. Different temperature probes are implemented in the simulation, to analyze relevant temperature profiles. Temperatures of the inner surface and outer surface (see Figure 14, right) are examined. In order to assure the integrity of the simulation, the temperature of the coating and the substrate material at the point of contact are compared.

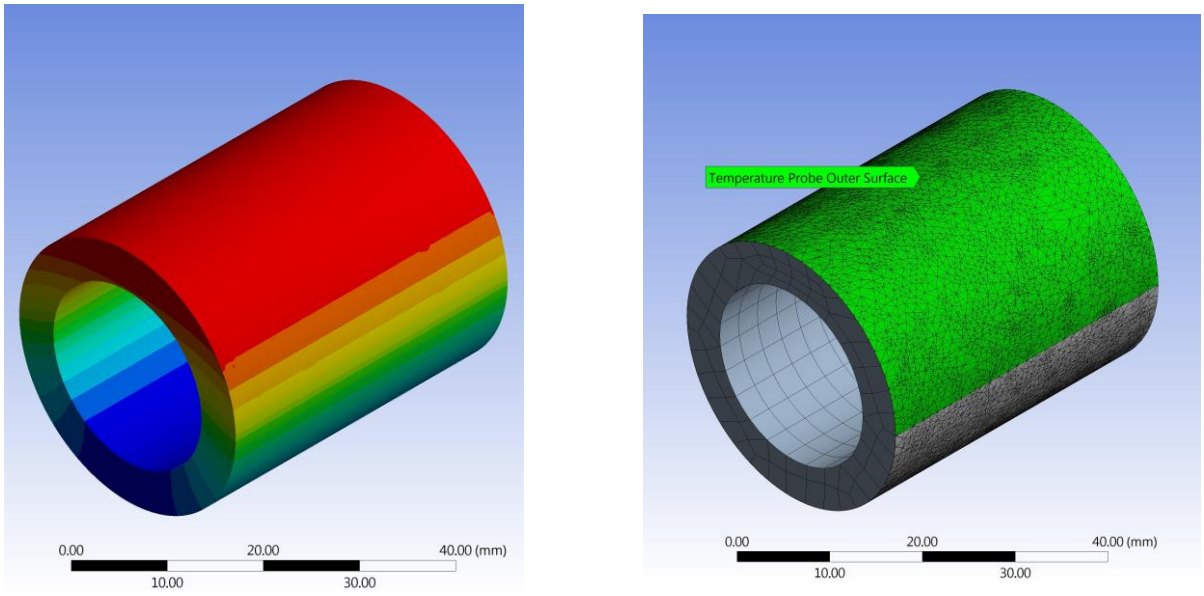

Figure 15: Example of simulation results; overall temperature distribution (left), surface temperature probe location and sample meshing (right).

To analyze the temperature distribution along a certain line, two temperature profiles have been issued within the scope of the simulation. A vertical temperature profile is used to consider the temperature gradient between the hottest point of the irradiated area and the inner surface beneath (Figure 16, left). Furthermore, a horizontal temperature profile along the irradiated half circumference is used to consider the surface temperature gradient between the center and the sides of the irradiated area (Figure 16, left). In a following step, it is also used to compare the results between both TMS.

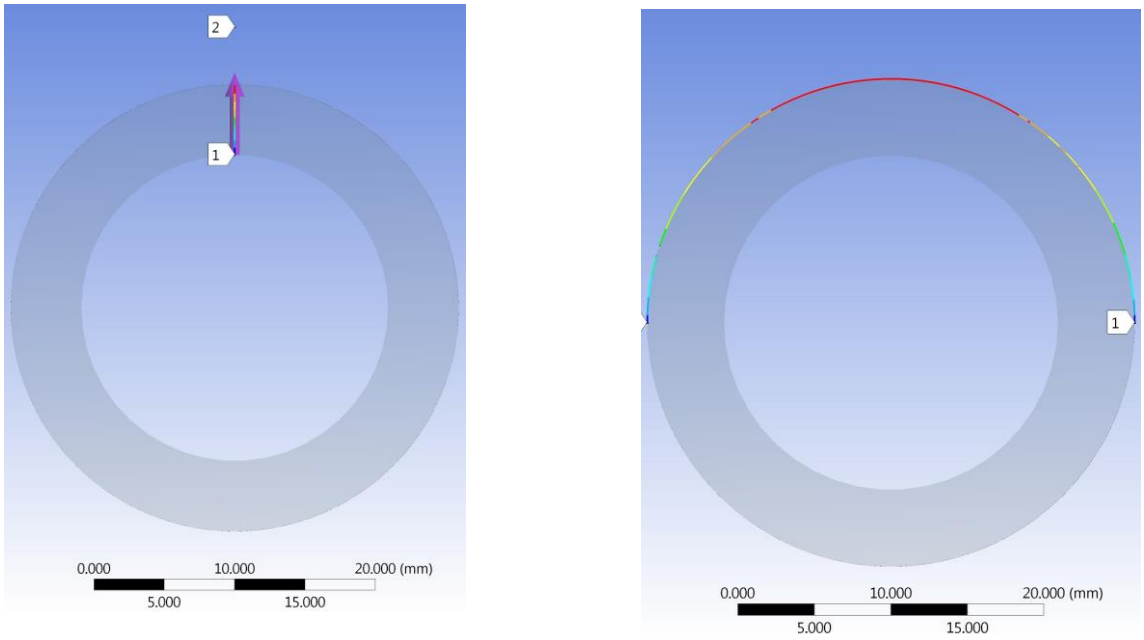

Figure 16: Cross-sided view of temperature profiles resulting from the simulation; vertically through the material (left) and horizontally along the irradiated surface (right)

A comparison between ANSYS simulation results and the analytical models that is used before leads to different deductions and enables a deeper understanding of the present temperature distribution. Conclusions on the applicability of both systems can be drawn and the remaining deviation can be assessed.

4. Contactless Temperature Measurement (TMS 2)

As mentioned in the previous chapter, a precise direct measurement of the sample surface temperature is not feasible due to irradiation of the sensor itself. Therefore thermocouples are placed beneath the surface, the heat loss between the measuring point and the sample surface are calculated and a temperature setpoint for the automated dish control system is derived (TMS 1). Within the scope of this thesis, a second temperature measurement system (TMS 2) with a different operating principle is implemented. The goal is to measure the thermal radiation emitted by the hot surface of the samples under concentrated solar flux in order to verify the derived temperature setpoint and to create a deeper understanding of the present temperatures.

4.1 Fundamentals and state of the art

In the following, a brief introduction to thermal radiation physics is given. The most important concepts are explained and fundamental approaches presented. Thereafter, the basics of infrared (IR) thermal imaging are introduced.

4.1.1 Thermal Radiation Physics

While in heat conduction and convection, the energy is transported by molecular processes or by macroscopic movement of fluids, the heat radiation is not bound to matter, but is based on electromagnetic processes. The intensity and type of radiation emitted by a gaseous, liquid or solid body depend on the nature and temperature of this body. Radiation has both wave and quantum properties. The wavelength λ is associated with the frequency ν via the speed of light c (see Equation 6) which is $c_0 = 2.998 \cdot 10^8\ m/s$ in vacuum.

$$\lambda = \frac{c}{\nu} \tag{6}$$

The electromagnetic spectrum (see Figure 17) shows that wavelengths in the area of thermal radiation range between $\lambda = 0.8\ \mu m$ and $\lambda \cong 20\ \mu m$. According to quantum theory, thermal radiation consists of photons that move at the speed of light and have no rest mass. Furthermore according to Planck, each photon transports the energy quantum E, which is equal to the frequency ν multiplied by Planck's constant ($h = 6.626 \cdot 10^{-34}\ Js$, see Equation 7).

$$E = h \cdot \nu \tag{7}$$

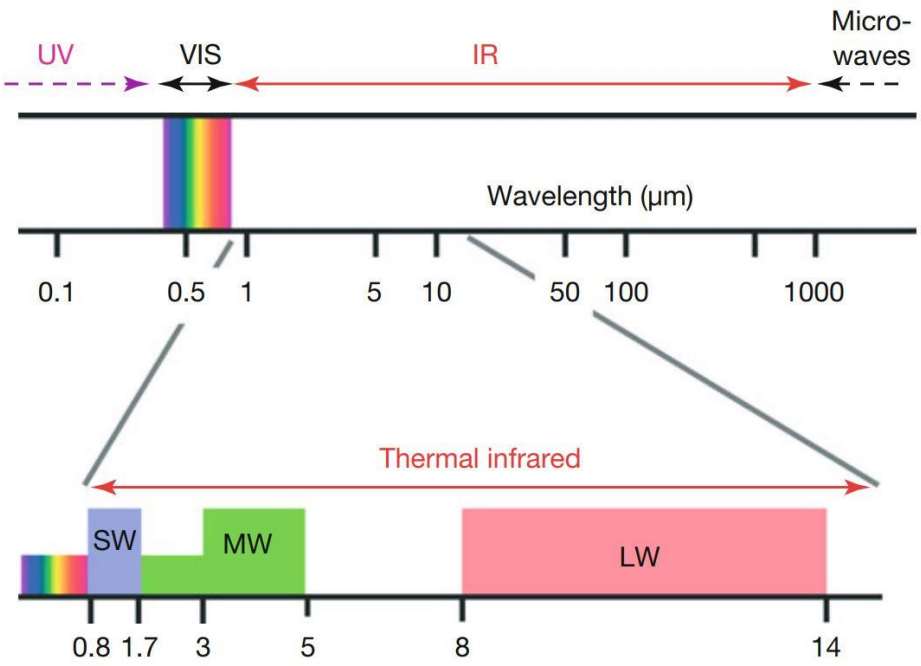

Figure 17: IR, adjacent spectral regions and expanded view of so-called thermal IR. Short-wave (SW), mid-wave (MW), and longwave (LW) subregions are indicated additionally[35]

Heat radiation does not only depend on the wavelength. In numerous problems, especially in the radiation exchange between different bodies, their spatial distribution must be considered as well. This applies to the emission of radiant energy in the same way as for reflection and absorption of radiation, which irradiates from a body surface.

The radiation emitted by a body surface covers a large wavelength range, its intensity depends on the absolute temperature of the body. The relationship between the total radiation emitted by a body and the absolute temperature can be formulated in particular for a blackbody. The blackbody is characterized by the following properties (see Figure 18):

1) A black body absorbs all incoming radiation, regardless of wavelength and direction.
2) For a given temperature and wavelength, no surface can emit more than the black body.
3) The emitted radiation of the black body is a function of temperature and wavelength, but independent of direction. The black body is an ideal diffuse radiator.

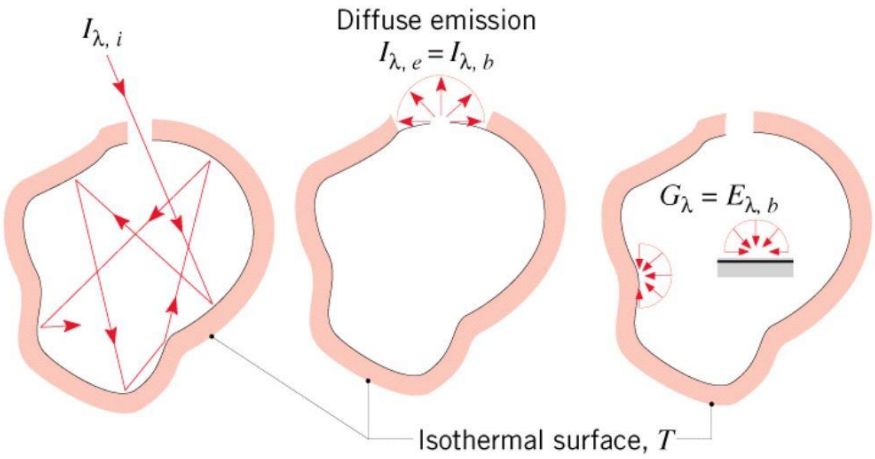

Figure 18: Characteristics of a black body: complete absorption (left), diffuse emission (center) and diffuse irradiation on inner surfaces (right) [36]

From quantum theory, Max Planck derived a relationship for the distribution of the radiation intensity of a black body over the wavelength. It can be expressed as shown in Equation 8: ($k = 1.3805 \cdot 10^{-23}\, J/K$).

$$\phi^{BB}(\lambda, T) = \frac{2\pi \cdot h \cdot c_0}{\lambda^5 \cdot (e^{\frac{h \cdot c_0}{k \cdot \lambda \cdot T}} - 1)} \tag{8}$$

For black bodies, the Stefan-Boltzmann law to calculate the thermal radiation applies. Therefore the Stefan-Boltzmann constant $\sigma = 5.67 \cdot 10^{-8}\, W/m^2K^4$ is multiplied by the temperature to the fourth power (see Equation 9).

$$\phi = \sigma \cdot T^4 \tag{9}$$

In the wavelength range considered for heat radiation, Planck's law of distribution is evaluated for various temperatures in Figure 19. It shows that the emitted radiation energy increases with increasing temperature and that the respective maximum intensity shifts to smaller wavelengths with increasing temperature. By differentiation of Equation 8, a relation for the position of the maxima at a certain wavelength can be given. It is known as Wien's displacement Law [36]:

$$\lambda_{max} = \frac{2897.8\ \mu m \cdot K}{T} \tag{10}$$

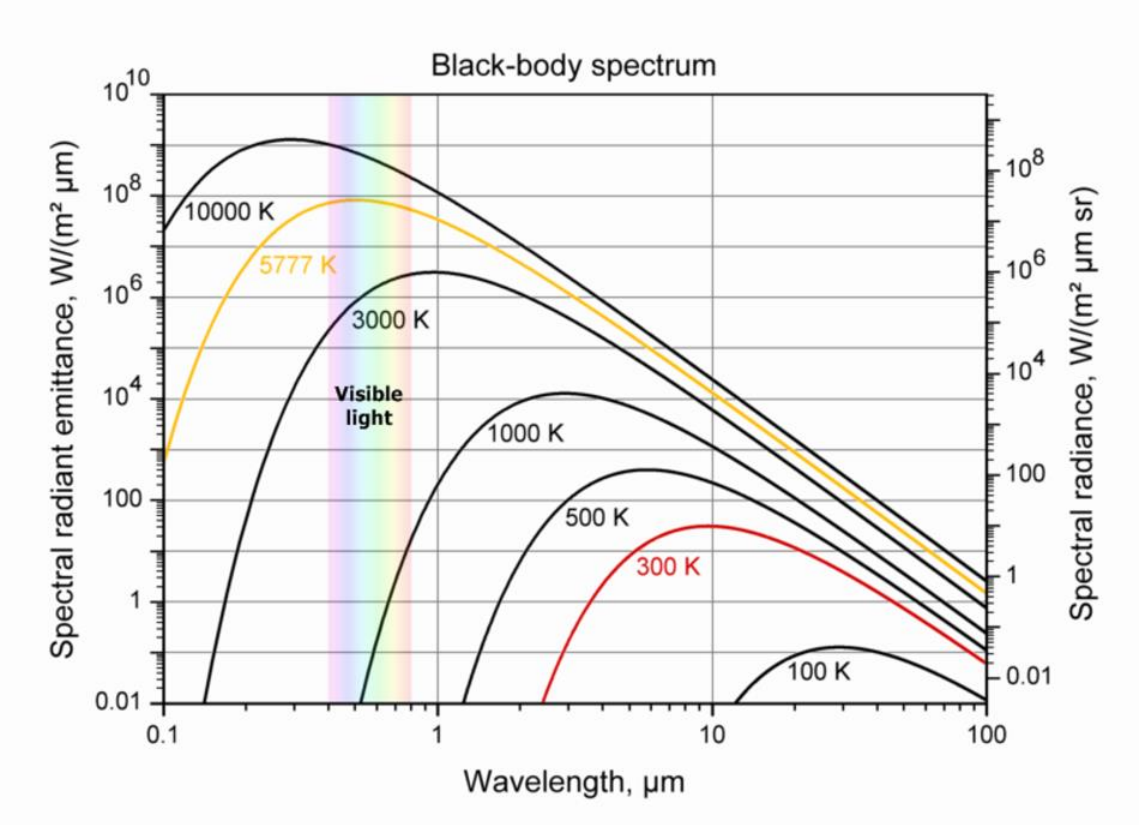

Figure 19: Radiation intensity of a black body at different temperatures [37]

If radiation (hereinafter referred to as Φ) strikes a body, it can be absorbed, reflected and transmitted. The absorptance α, reflectance ρ and transmittance τ of a body depend on temperature, chemical composition and surface texture of the body as well as on the polarization of the radiation. These factors are also dependent on wavelength λ. From the law of conservation of energy, it follows [38]:

$$\alpha + \rho + \tau = 1 \tag{11}$$

Kirchhoff's law describes the relationship between the absorbed and emitted radiation of a body. No real surface possesses a higher emittance than a black body with the same temperature [36]. The law is stated as:

$$\varepsilon(\Omega, \lambda, T) = \alpha(\Omega, \lambda, T) \tag{12}$$

4.1.2 Infrared Thermal Imaging

Thermography is an imaging technique for measuring and displaying radiation temperatures. By means of a thermal imaging camera (also called a thermal or IR camera), the IR radiation emanat-

ing from a surface is measured. From the IR radiation, the temperature (radiation temperature) of a surface can be calculated.

A thermal detector converts IR radiation into an electrical signal and thus represents the core component of an imaging IR system. Thermal detectors can be divided into two groups: photoelectric (quantum) detectors and thermoelectric detectors. They differ in their mode of action. In a thermoelectric radiation detector, incident radiation is absorbed, resulting in a temperature change. This causes the change of an electrical quantity (e.g. conductivity), which is then measured at a detector element. With the photoelectric radiation detector, the incident radiation directly solves electrons from the valence band of the semiconductor detector and thereby generates electrical charge carriers. This effect is also called inside photoelectric effect [38].

Thermal detectors are arranged in a focal plane array (FPA) where incident radiation is converted to an electrical signal corresponding to the size of the FPA that is conforming with the pixel size of the thermal image crated thereafter. With knowledge about the size of the FPA and the installed optics, a field of view (FOV) that represents the dimensions of an observed plane area at a certain distance can be derived (more information can be found in the Appendix). The optics and the installed optical filters furthermore determine the bandwidth and the central wavelength of detected radiation. Another important figure to classify an IR camera is the number of captioned frames per second (framerate) and the time the detector takes to response to changes in the recorded image (integration time). Specific values for the camera that used in the scope of this thesis can be found in Table 3.

The basic measurement process in radiation thermometry is described using the concept of the radiometric chain. It includes all phenomena that affect the detection of the radiation emitted by an object at a given temperature (see Figure 20). The radiometric chain begins with the emittance of heat radiation through the object at a temperature T_{object}. To describe different radiant power contributions to the detector signal, the expression ϕ_i is used, whereas i indicates the contribution mechanism. The radiant power of the object $\phi_{object}(T_{object})$ compared to the radiant power of a blackbody $\phi_{object}^{BB}(T_{object})$ is given by

$$\phi_{object}(T_{object}) = \varepsilon_{object} \cdot \phi_{object}^{BB}(T_{object}) \tag{13}$$

The reflectance of the opaque grey object is given by

$$\rho = 1 - \varepsilon \tag{14}$$

The object receives thermal radiation from its surrounding at ambient temperature T_{amb} and reflects the radiant power:

$$\rho_{object} \cdot \phi_{amb}(T_{amb}) = \left(1 - \varepsilon_{object}\right) \cdot \phi_{amb}(T_{amb}) \tag{15}$$

The radiant power emitted and reflected by the object towards the camera is passing through the atmosphere. Because of the absorption and scattering processes in the atmosphere, the radiant power is further attenuated. This can be quantified by multiplying the radiant power contribution from the object and the surroundings by the atmospheric transmittance τ_{atm}. If it is assumed that the atmospheric transmittance is dominated by absorption losses only (scattering mechanism neglected), the atmosphere at a temperature T_{atm} will also emit a radiant power $(1-\tau_{atm}) \cdot \phi_{atm}(T_{atm})$. Therefore, the camera detects a radiant power mixture with contributions from the object, the surroundings, and the atmosphere. The total radiation power incident on the detector ϕ_{det} can be written as

$$\phi_{det} = \tau_{atm} \cdot \varepsilon_{object} \cdot \phi_{object}^{BB}(T_{object}) + \tau_{atm} \cdot (1-\varepsilon_{object}) \cdot \phi_{amb}(T_{amb}) + (1-\tau_{atm}) \cdot \phi_{atm}(T_{atm}) \tag{16}$$

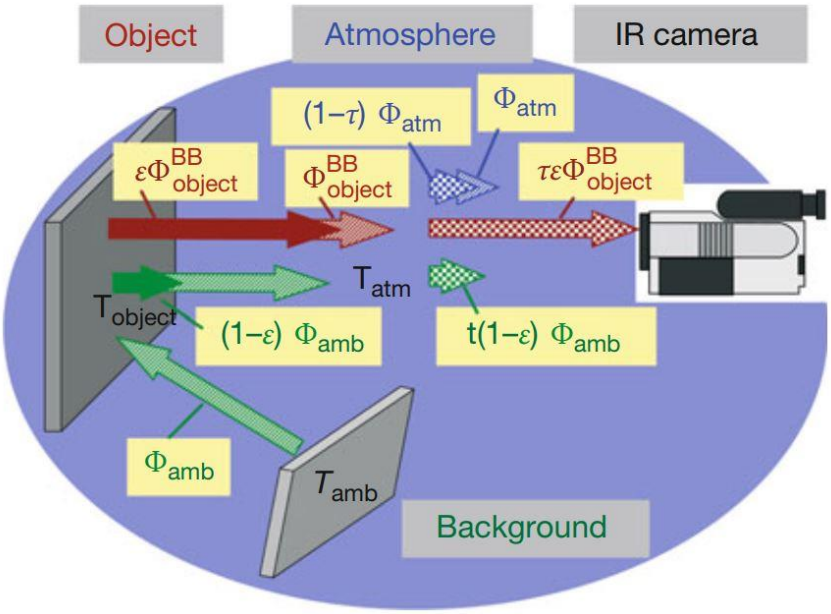

Figure 20: Radiometric chain – IR camera measurement process and influencing phenomena [35]

Equation 16 represents the radiant power. For the calculation of the detector signal, it has to be integrated over the wavelength. This accounts for the spectral dependence of detector responsivity, atmospheric transmittance and object emittance. For blackbody radiation and short measurement distances, the emittance ε and the atmospheric transmittance τ_{atm} can be set equal to one. This is used to calibrate the infrared camera with a black body radiator [35].

4.1.3 Specific radiometric chain and solar blindness calculation

To conduct successful thermographic measurements of hot object surfaces under concentrated solar flux, several modifications to the standard setup of a radiometric chain have to be carried out. Furthermore, through a separation of the radiation emitted by the surface of the hot object (“signal”) and the signal contribution from solar radiation (“noise”), a statement about the cameras susceptibility to solar radiation (solar blindness) can be made.

Figure 21 shows an exemplary illustration of the radiometric chain of an examined object under concentrated solar flux. Solar radiation (1) passes through the atmosphere and is attenuated by the atmosphere (2). After being reflected and concentrated by a (parabolic) mirror (3), the radiation is partially absorbed by the examined object. The remaining fraction (4) is reflected by the opaque object and after passing the camera’s optics, it reaches the detector as “noise” (5). The thermal radiation emitted by the measured object surface itself (A) only passes the cameras optics and reaches the detector as “signal” (B). Through calculating the fluxes and weighting the spectra with the bandwidth of detector, a “signal-to-noise” ratio can be derived. In this way, the cameras solar blindness can be assessed. An estimation for the equipment used in the scope of this thesis is presented in the following chapter.

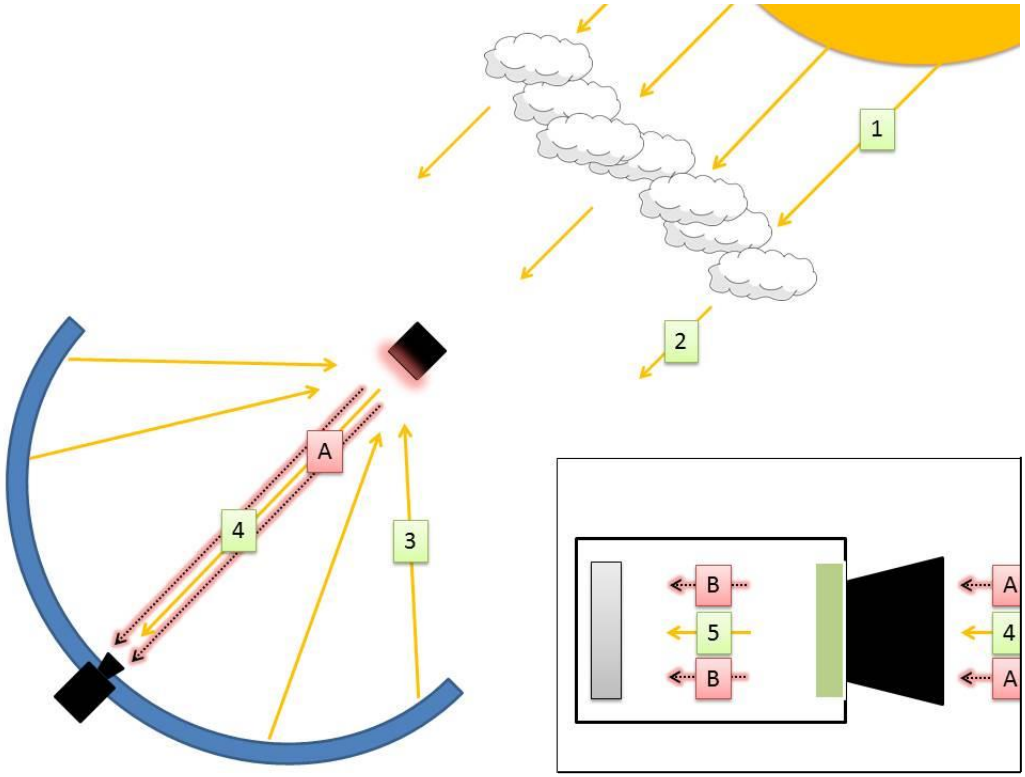

Figure 21: Exemplary illustration of the radiometric chain of an examined object under concentrated solar flux [39]

4.2 Infrared Camera Setup

In the following, a brief introduction into the IR camera system that is used in the scope of this thesis is given. First, the hard- and software components are explained, then a solar blindness assessment is carried out according to the aforementioned scheme. At last, the calibration and assembly of the camera system is described.

4.2.1 Hardware

Thermal images are taken with an *Optris PI 640 G7*. Camera properties are displayed in Table 3:

Table 3: Properties of *Optris PI 640 G7* camera [40]

Property	**Value**
Image Size	640 x 480 pixels
Spectral range	7.95 µm, FWHM: 0.35µm (see Figure 23)
Detector Type	UFPA
Framerate	max. 32 Hz
System accuracy	max (2 °C or 2 %)
Warm-up time	10 min
Temperature range	Sighting range: 0 - 250 °C Measurement range: 200 - 1500 °C
Objective	15° x 11° FOV / f = 41.5 mm

To protect the camera against direct solar irradiation, precipitations and temperature fluctuations, it is mounted inside a protective housing (see Figure 22). Besides the camera, the housing contains a USB server to be able to feed the camera data directly into a local network and a temperature regulation unit. This unit includes a fan to circulate the air inside the closed housing and a heating unit that is activated at a temperature below $15\,°C$ [40]. Furthermore the lens and the front end of the camera housing are protected by a germanium window. Due to its narrow band pass filter, only radiation of wavelengths inside the certain spectral range of the area is able to pass through (see Figure 23).

Figure 22: *Optris PI 640 G7* infrared camera (grey cube at the left) inside the protective housing. Furtermore, the USB-Server (blue), the heating unit (below the USB server) and the protective germanium window is visible [40].

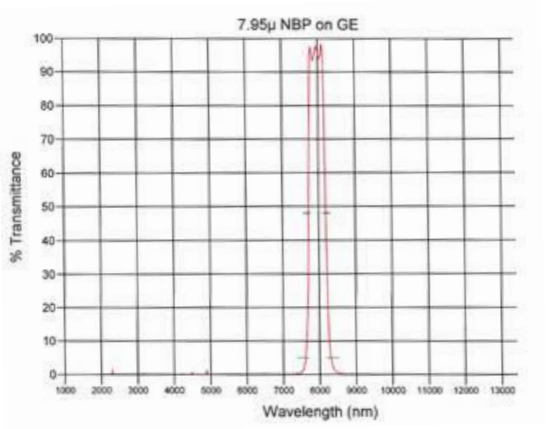

Figure 23: Transmittance of camera objective at $7{,}95\ \mu m$ narrow band pass (NBP)

4.2.2 Software

The creation and evaluation of thermal images is carried out using the software *Optris PI Connect* (see Figure 24). Different values for ambient temperature, IR-window transmittance, object emittance, flag (shutter control), framerate, etc. can be set. Furthermore, measurement areas of a different shape can be defined. In the scope of this thesis, IR images with a defined IR-window transmittance of $\tau_{IR-window} \cong 0.91$, an ambient temperature of $25\ °C$ and various predefined emittance values are created. Reference images are taken with an emittance set equal to one. It is either possible to issue an image data file in *Tagged Image Format* (".tiff") containing image data and temperature data or a table of temperature data is *Comma-sperated Value Format* (".csv").

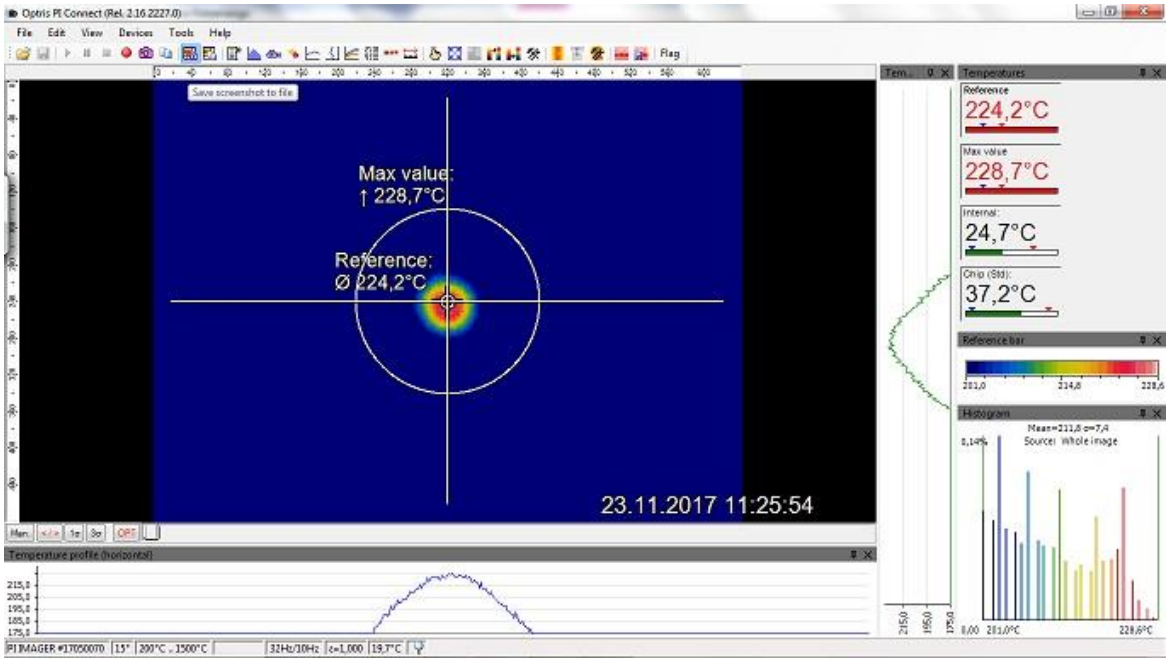

Figure 24: Screenshot of Optris PI Connect thermal imaging software during blackbody calibration procedure before focusing the camera objective

In a second step, image processing is done using *MATLAB*. Temperature table data is connected to sample location by the definition of a central pixel for each sample. Thus, measurement areas can be created and various images can be compared to each other. The emitance value in the wavelength spectrum of the IR-Camera ε_{IR} is used to create one thermal image for each sample. At last a composite analysis is carried out, using the predefined measurement areas of each thermal image created with the specific ε_{IR} value of each sample.

4.2.3 Solar blindness assessment

Before reliable infrared thermal image data can be collected, the solar blindness of the camera has to be assured qualitatively as described in chapter 4.1.3. As mentioned before, the wavelength of measurement of the Optris camera ranges from 7.55 to $8.35\ \mu m$. Therefore, all calculations have to be related to this certain spectral range.

The first step in calculating the possibly occurring “noise” in a measurement is to take a look at the extraterrestrial solar spectrum. The overall flux density of solar irradiance is also known as the *solar constant*, and amounts roughly to $1361\ W/m^2$. From *Standard Solar Constant and Zero Air Mass Solar Spectral Irradiance Tables (*ASTM-Standard no. E490) [41], the fraction of solar irradiance in the aforementioned wavelength range can be calculated. This corresponds to $0.041\ \%$ of the solar constant, which results in $\sim 0.56\ W/m^2$. As visible in Figure 25, the major part (95%) is irradiated at smaller wavelengths, mostly in the UV-VIS-NIR range from 0.3 to $2.5\ \mu m$.

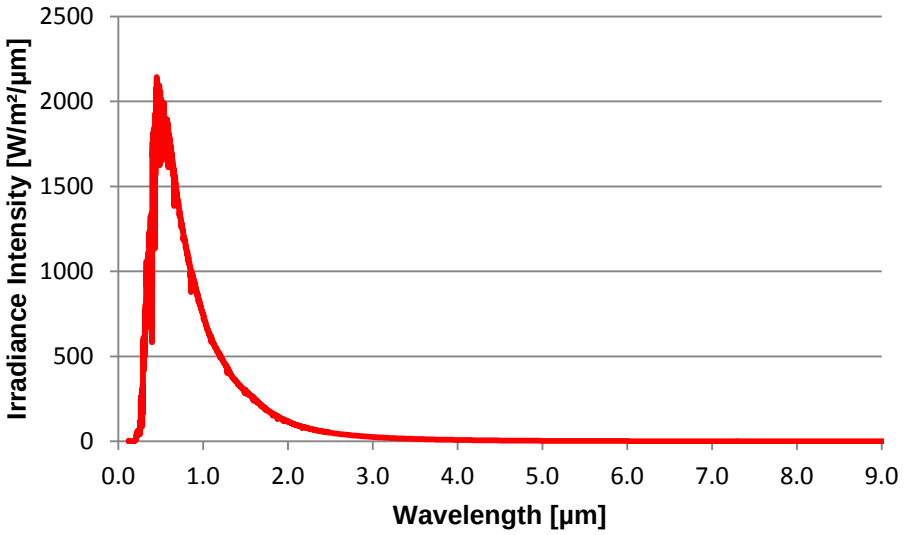

Figure 25: Extraterrestrial Solar Spectrum [41]

The next step is the approximation of atmospherical transmittance in the aforementioned wavelength range. A tool called *MODTRAN* is used to derive transmittance values depending on wavelength, geographical position and other factors (see [42]). Only an average of 29% of solar radiation is transmitted in the considered wavelength area, attenuating the radiation value to $\sim 0.16\ W/m^2$.

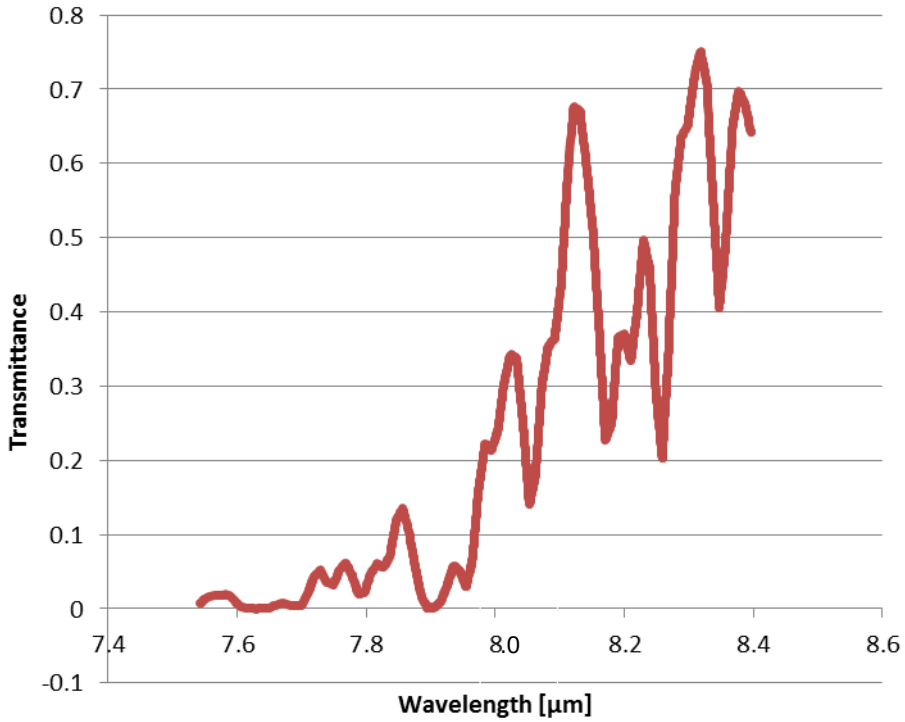

Figure 26: Atmospheric transmittance values derived from *MODTRAN* with a sensor altitude of 50 km, sensor zenith of 180 °, ground temperature of 21 °C and *Mid-Latitude Summer* Atmosphere Model *[42].*

After passing the atmosphere, the solar radiation is reflected and concentrated through a parabolic mirror. The reflectance of a standard mirror is measured using a *Perkin Elmer Frontier Fourier Transform Infrared (FTIR*) spectrometer, with a diffuse gold coated $76.2\ mm$ integrating sphere and incidence angle of 12 °, delivered by *Pike Ltd. Technologies* (see Figure 27). First, the hemispherical reflectance is measured, then the specular part is excluded, thus recording the diffuse reflection. The specular reflectance of the mirror is negligible from $\lambda = 7{,}55\ \mu m$ to $\lambda = 8{,}25\ \mu m$, then raises linearly up to $4\ \%$ at $\lambda = 8{,}35\ \mu m$. The mirror thus absorbs most of the IR radiation. Nevertheless, the residual solar reflection is enhanced by the concentration factor of the parabolic dish system. The maximum values for the test campaign at the dish is about $x350$, leading to an overall decrease of radiation of $-12.5\ \%$. This reduces the already very small intensity value of the radiation from $\sim 0.16\ W/m^2$ to $\sim 0.14\ W/m^2$.

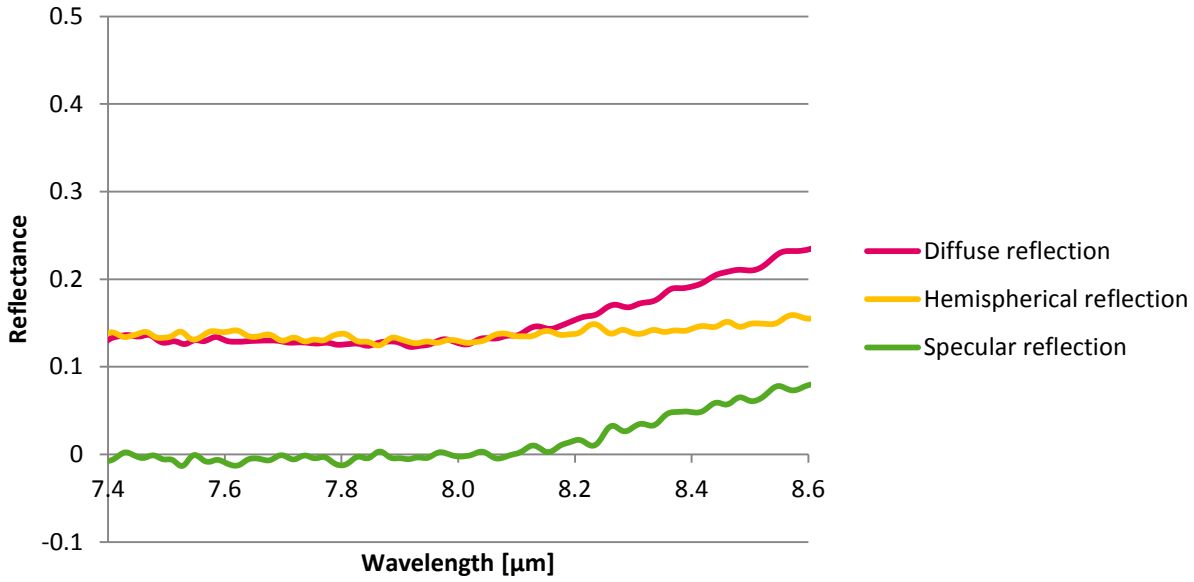

Figure 27: Reflectance values of a reference mirror

Using the same equipment and procedure, a reflectance measurement of a representative black-coated flat sample surface is carried out. The spectrum is depicted in Figure 28. It can be seen that the average reflectance in the considered wavelength range is below $20\ \%$.

The radiation creating the signal and the radiation creating the noise of the detector signal both have to pass through the camera optics. Therefore this last step of solar blindness calculation can be skipped, since a ratio is derived. According to Plack's law, the blackbody band irradiation for wavelengths from $7.55\ \mu m$ to $8.35\ \mu m$ and a temperature of $1000\ K$ (rougly the temperaure setpoint for dish tests) is equal to $589.63\ W/m^2$, which is three orders of magnitude larger than the residual solar reflection. For this reason, the signal-to-noise ratio calculation is aborted at this point. It can be stated that for the aforementioned circumstances, solar blindness is confirmed and only a negligible part of solar radiation reaches the detector of the camera system.

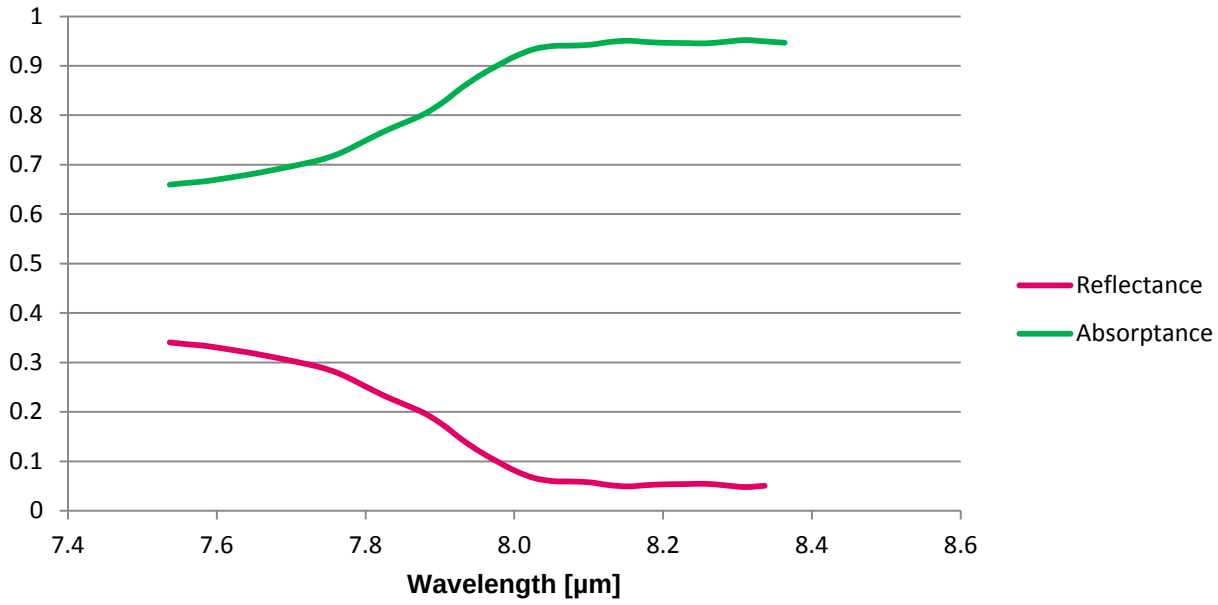

Figure 28: Reflectance and absorptance values of a representative black-coated flat sample

In the past, tests regarding this subject have already been conducted at the *Plataforma Solar de Almería*. Infrared cameras with different band-pass filters centered at $3320\,nm$ and $4720\,nm$ have been used to quantify measurement errors on hot sample surfaces with different emittance values [30]. The results are depicted in Figure 29. At $3320\,nm$, the relative temperature measurement error for a black coating (Reflectance: 0.1 at $1000\,K$) is about $0{,}1\%$. At $4720\,nm$, this relative error further decreases to $0{,}01\%$. For a selective coating with a reflectance of 0.9, the relative error is two orders of magnitude higher.

With the higher emittance values of conventional black-coated samples, the first term of Equation 16 that focuses on the radiation of the object itself plays a more important role than the second term that depicts the reflected signal by the surroundings.

Regarding Kirchhoff's law it is visible in Figure 29, that black coatings (with a reflectance of below 0.1) tend to create a lower level of infrared temperature measurement errors at different temperatures and wavelengths than higher reflecting surfaces. Hence, selective coated samples (see Appendix) with lower emittance and therefore higher reflectance values show a presumably higher sensitivity to measurement errors and create a more significant error term when calculating the total radiation power incident on the IR-camera detector.

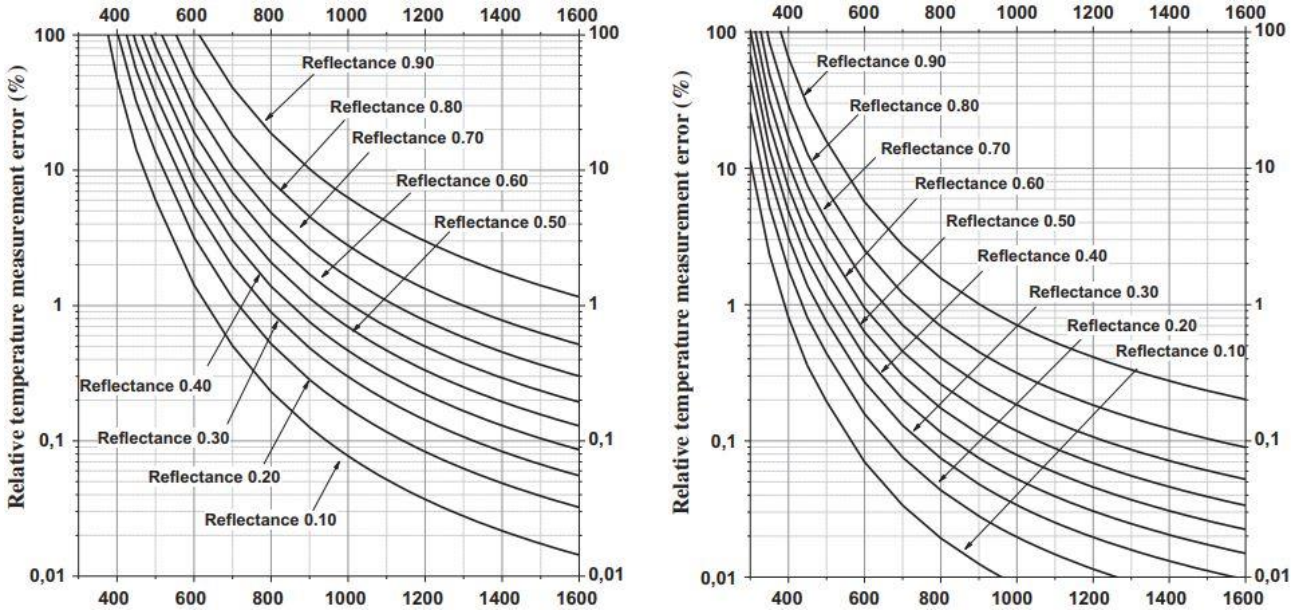

Figure 29: Relative temperature measurement at different temperatures [K] errors using band-pass filters centered at $3320\ nm$ (left) and $4720\ nm$ (right) according to the sample reflectance [30].

4.2.4 Laboratory calibration tests

To confirm the predefined calibration values and to familiarize with the IR camera system, several tests are conducted before field testing. In a first step, the transmittance value for the germanium protective window is adjusted. A *Lumasense MIKRON M335* blackbody calibration source with a circular aperture (diameter of $16\ mm$) is operated at different temperatures ($500, 550, 600\ °C$). The camera is positioned 1 m apart from the blackbody. During various measurement steps either with or without the protection window, an IR-window transmittance value of 0.91 can be confirmed.

To replicate the conditions of subsequent camera application at the dish facility, a selfmade blackbody radiation source is built (see Figure 30). A metallic plate is painted with *Pyromark 2500* and mounted to a muffle furnace receiving heat from the backside. The present temperature at the surface is then measured with three thermocouples (at the outer side, inner side and the edge of the metal plate) and used to determine a temperature set point of the furnace. Although its emittance is not as well known as for the blackbody source, the camera target has a larger area at a homogeneous temperature. Thermal measurements with different IR cameras at distinct measuring distances show an attenuating temperature at increasing measurement distances. This leads to a measurement error of approximately $20\ °C$ at $500\ °C$ and $5\ m$ of distance, exceeding the specified tolerance of measurements by $10\ °C$ (2%).

In a last step, the irradiating area of the blackbody calibration source is reduced to determine an influence of object size coupled with increasing distance on the thermal image outcome. At temperatures of 600, 700 and $800\ °C$ and measuring distances of 1, 3 and $5\ m$, thermal images of the blackbody source opening are taken, which is decreased in diameter from $16\ mm\ to\ 4\ mm$ in steps of $2\ mm$. The results are presented in Chapter 5.2.

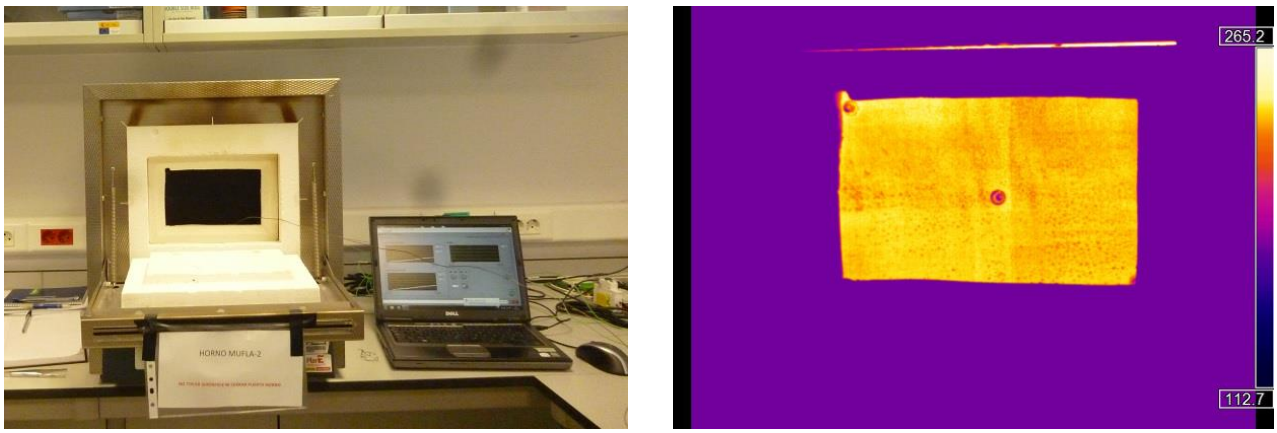

Figure 30: Selfmade Blackbody radiation source: Image of setup (left) and exemplary thermal image taken with *Optris* camera during the test (right)

4.2.5 Installation

Figure 31 illustrates the mounting of the IR camera. From the central spot of the parabolic-shaped mirror, the camera faces towards the samples at a distance of approximately $5\ m$. A mobile elevating work platform that is also used for mirror-cleaning services at the PSA is navigated to the aforementioned spot with the dish system settled in its upside down rest or “stow” position, where the camera is mounted looking towards the test bench. Power and network access is ensured by previously laid cables. The USB server is able to work with *Power over Ethernet*, though the temperature regulation unit is powered with $24\ V\ DC$. Gigabit Ethernet is used for image transfer.

Figure 31: Predefined camera mounting point at the center of the dish (red circle, left) and close-up of the mounted camera (right)

4.3 Review of optical sample characterization

As mentioned previously, the dish cycling routine also consists of a periodical optical characterization of sample surfaces. The solar absorptance α_{sol}, the thermal emittance ε_{th} and the emittance in the wavelength spectral range of the IR-Camera ε_{IR} are the most important figures.

To determine α_{sol}, the spectral hemispherical reflectance $\rho(\lambda)$ is measured at room temperature using a *Perkin Elmer Ultraviolet Visible Near-Infrared (UV-VIS-NIR) Lambda 1050 spectrophotometer*, with a $150\,mm$ integrating sphere and an incidence angle of $8\,°$. Spectral measurements are conducted in $5\,nm$ steps from $0.28\,\mu m$ to $2.5\,\mu m$. Each coated sample is measured at three positions. The solar absorptance α_{sol} is calculated according to Equation 17 by weighting spectral measurements with the ASTM G173-03 reference spectrum for solar direct normal irradiance $G_{sol}(\lambda)$ at an air mass (AM) of 1.5 (see Figure 32).

The integrands in the numerator and denominator are discretized into wavelength bands to accommodate the available data and then summed to approximate the integrals, i.e. $\lambda_1 = 0.28\,\mu m$; $\lambda_2 = 25\,\mu m$; $d\lambda = 0.005\,\mu m$.

$$\alpha_{sol} = \frac{\int_{\lambda 1}^{\lambda 2}[1-\rho(\lambda)]\cdot G_{sol}(\lambda)\cdot d\lambda}{\int_{\lambda 1}^{\lambda 2} G_{sol}(\lambda)\cdot d\lambda} \tag{17}$$

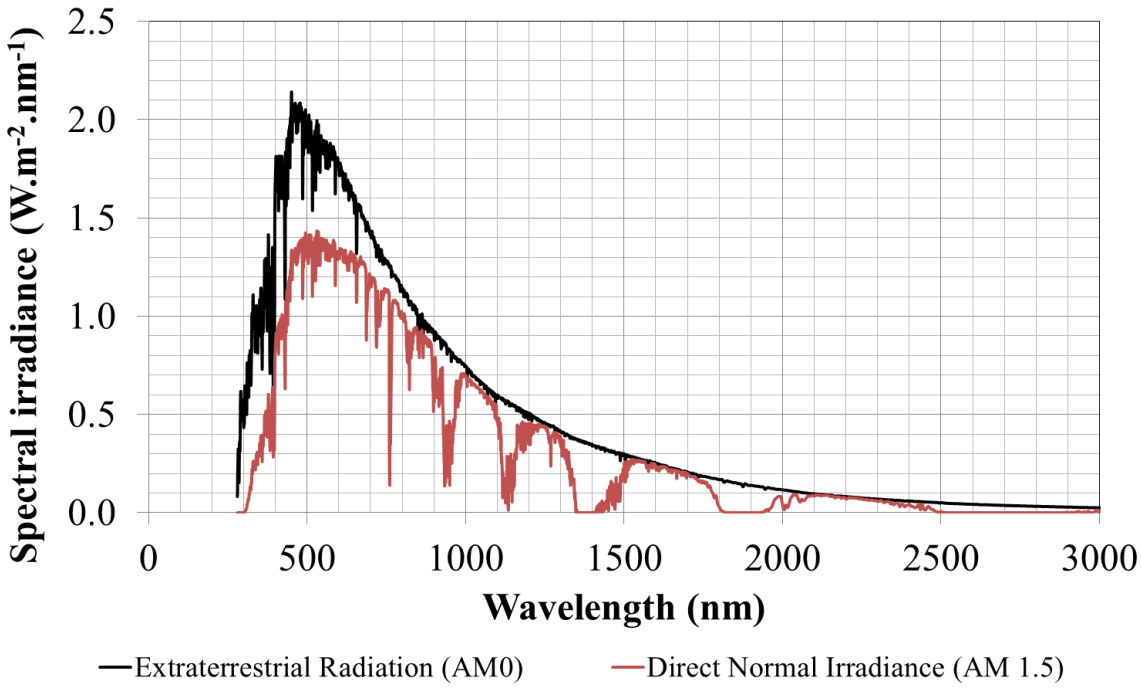

Figure 32:ASTM G173-03 solar spectral irradiance reference spectra [29]

To determine ε_{th} and ε_{IR}, the spectral hemispherical reflectance $\rho(\lambda)$ is measured at room temperature using the aforementioned *Perkin Elmer Frontier-FTIR spectrophotometer*. Spectral measurements are performed in $0.004\ \mu m$ steps from 2 to $16\ \mu m$. Each coated sample is measured at three positions. Sample reflectance measurements $R_s(\lambda)$ are contrasted with the measurements for a reference standard as a baseline $R_r(\lambda)$. Furthermore, this quotient is multiplied with a reference spectrum $\rho_r(\lambda)$:

$$\rho(\lambda) = \frac{R_s(\lambda)}{R_r(\lambda)} \cdot \rho_r(\lambda) \tag{18}$$

A spectral mismatch is observed when comparing UV-VIS-NIR and raw FTIR data in the wavelength range from $2\ \mu m$ to $25\ \mu m$. This mismatch depends on the type of coating, its origin is not yet explained. The thermal emittance ε_{th} is calculated at any temperature $T\ (K)$ according to Equation 19, by weighting spectral measurements from $\lambda_1 = 0.28\ \mu m$ to $\lambda_3 = 16\ \mu m$ with the corresponding blackbody radiation spectrum, defined by Planck's law (see Equation 8) [29].

$$\varepsilon_{th}(T) = \frac{\int_{\lambda 1}^{\lambda 2}[1-\rho(\lambda)] \cdot \phi^{BB}(\lambda, T) \cdot d\lambda}{\int_{\lambda 1}^{\lambda 2} \phi^{BB}(\lambda, T) \cdot d\lambda} \tag{19}$$

The emittance in the wavelength spectrum of the IR camera ε_{IR} is calculated in a similar way (see Equation 20). In this case, it is done by weighting spectral measurements from $\lambda_3 = 7.55\ \mu m$ to $\lambda_4 = 8.35\ \mu m$ with the corresponding blackbody radiation spectrum

$$\varepsilon_{IR}(T) = \frac{\int_{\lambda 3}^{\lambda 4}[1-\rho(\lambda)] \cdot \phi^{BB}(\lambda, T) \cdot d\lambda}{\int_{\lambda 3}^{\lambda 4} \phi^{BB}(\lambda, T) \cdot d\lambda} \tag{20}$$

5. Results

In the following, the outcomes of the aforementioned experiments are presented. Two samples, one coated (number 89) and one uncoated sample (number 73) have been selected to exemplarily depict the different results. Other samples are further documented in the Appendix. As displayed in Figure 10, the position of the coated exemplary sample is at the center of the second line, whereas the uncoated exemplary sample is positioned at the outlet of the first line. Both samples have been selected as being representative for the particular group due to the average outcome of their test results.

5.1 TMS 1

The results of the ANSYS simulation for the exemplary samples are depicted in Table 4. The imput values are the thermal emittance ε_{th}, the solar absorptance α_{sol}, the thermocouple temperature, the measured distance from the thermocouple to the sample skin and the incident solar radiation. Furthermore, the thermal conductivity of the ceramic coating (set constant to be $0{,}487\ \mathrm{W/m \cdot K}$) and the temperature-dependent thermal conductivity of the substrate material (to be found in the Appendix) are considered. While keeping all other parameters constant, the convection coefficient from the inside surface to the fluid ($h_{int \rightarrow f}$ value) is derived iteratively during the simulation, so that the temperature reading at the thermocouple position corresponds to the measured value.

For the uncoated sample number 89, a skin temperature of $749\ °C$ is found out, resulting in a difference between thermocouple and skin temperature (ΔT_{ANSYS}) of $35.6\ °C$. The temperature on the inside surface of the tubular sample is found out to be $673.3\ °C$, resulting in a temperature difference between thermocouple and inside surface of $75.7\ °C$. Moreover, for the coated sample, a temperature of the interface between substrate and coating material is derived ($T_{interface} = 732.\ °C$). This corresponds to a temperature difference of $16.98\ °C$ over the coating thickness.

The uncoated sample number 73 shows a slightly lower skin temperature of $724.9\ °C$ even though the measured temperature of the thermocouple is similar. A difference between thermocouple and skin temperature (ΔT_{ANSYS}) of $13.2\ °C$ is calculated. The temperature on the inside surface of the tubular sample is found out to be $666.6\ °C$, resulting in a temperature difference between thermocouple and inside surface of $58.3\ °C$.

Table 4: Imput values, derived convection coefficient and output values of ANSYS simulation (exemplary samples)

Sample Number	**89**	**73**
Thermal Emittance ε_{th} [%]	0.84	0.62
Solar Absorptance α_{sol} [%]	0.97	0.91
Temperature Thermocouple T_{TC} [°C]	713.4	711.7
Distance Thermocouple from Skin [mm]	1.65	1.20
Solar Flux Q_{sol} [W/m²]	333.6	226.3
Convection coefficient $h_{int\rightarrow f}$ [W/m²·°C]	416	438.7
Skin temperature $T_{final,\ TMS1}$ [°C]	749	725
Interface temperature $T_{interface}$ [°C]	732	-
Inside surface temperature $T_{inside\ surface}$ [°C]	673.3	666.6
ΔT_{ANSYS}: (Skin↔Thermocouple) [°C]	**35.6**	**13.2**
ΔT: Skin↔Interface [°C]	17	-
ΔT: Skin↔Inside Surface [°C]	75.7	58.3

Figure 33 shows a graphic comparison of the process of surface temperature assessment using TMS 1 for both exemplary samples. A higher ΔT_{ANSYS} value for the coated sample is added to the similar thermocouple temperature, resulting in a higher final surface temperature of the coated sample.

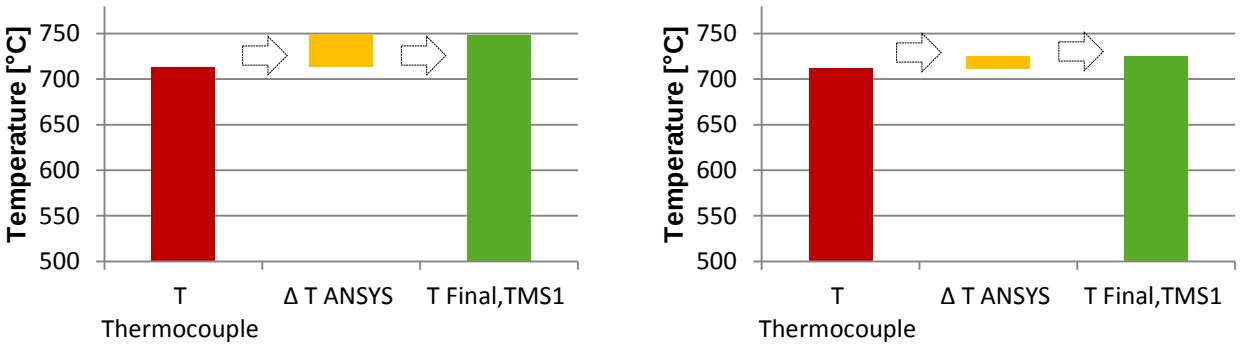

Figure 33: Temperature assessment using TMS 1 for exemplary samples number 89 (left, coated) and 73 (right, uncoated)

5.2 TMS 2

5.2.1 Calibration results

The results of the IR camera calibration at varying distances and object sizes at a blackbody temperature of 700°C are presented in the following. Additional results can be found in the Appendix.

At a steady distance, the measured temperature decreases constantly with decreasing object size (see Figure 34). Additionally at increased measurement distances, a decreasing measured value for the same object size is detected. If measured object size falls below the Imaging Field of View (IFOV) of the camera, which is the minimal object size that is necessary to detect a reliable temperature, measured values are severely disturbed.

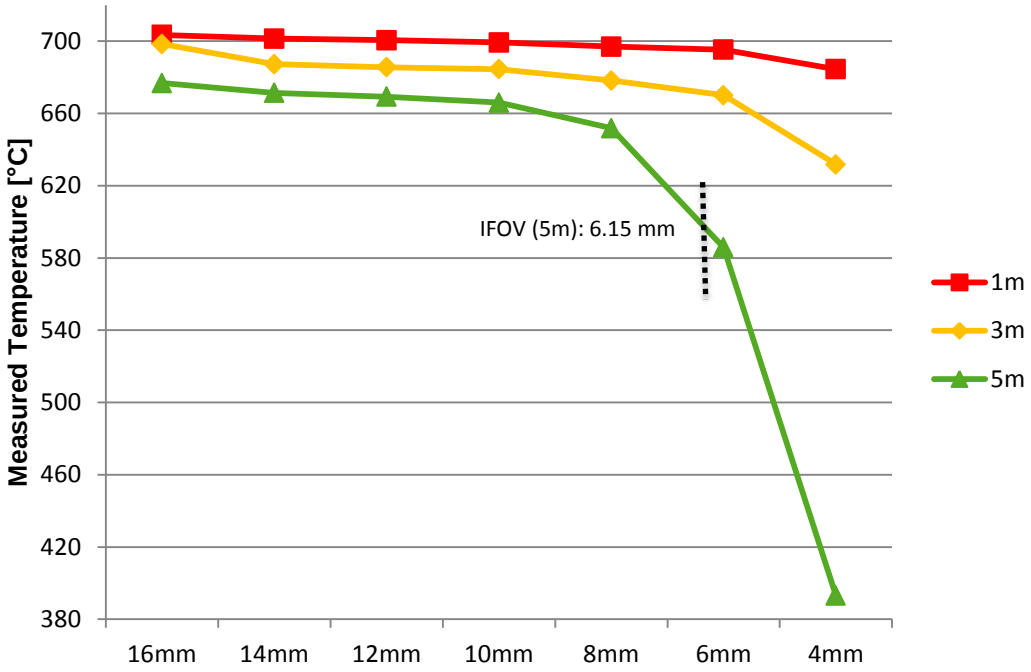

Figure 34: Measured temperatures at varying distances and area sizes of the blackbody radiation source at a temperature of 700 °C

5.2.2 Emittance values

For the extraction of correct IR images the thermal emittance of the samples in the corresponding wavelength band of the camera, ε_{IR} has to be measured and calculated according to the aforementioned procedure. Before testing and after every 25 cycles, an optical characterization of all samples is carried out. Table 5 gives an insight of the ε_{IR} value derivation for the coated exemplary sample number 89 at zero and after 25 passed cycles. The IR Image that is considered for further calculations is taken during the 12th cycle (see Figure 36). Therefore, the values of the two mentioned cycles are averaged.

At three different measuring positions ($0\,°$ and $45\,°$-turn in positive and negative direction) and at three different setpoint temperatures ($700\,°C$, $750\,°C$, $800\,°C$) ε_{IR} values are calculated. Due to the minimal fluctuations of the values it can be stated, that ε_{IR} values for coated samples are constant over the considered measured position and temperature range. Moreover, coated samples seem to be impervious to the impacts of solar radiation, due to a minimal decrease after 25 cycles (third decimal place of ε_{IR} values). Since the dish cycling setpoint is intended to be 750 °C, the overall average value for this temperature is used as final ε_{IR} value for the weighting of each sample with the respective emittance in the IR image (marked in bold).

Table 5: ε_{IR} values at different temperatures, measuring positions and cycle counts for coated sample number 89

Sample 89 at 0 cycles	**T=700 °C**	**T=750 °C**	**T=800 °C**
Position 1	0.900	0.900	0.900
Position 2	0.899	0.899	0.899
Position 3	0.897	0.897	0.897
Average	0.899	0.898	0.898
Standard Deviation	0.001	0.001	0.001

Sample 89 at 25 cycles	**T=700 °C**	**T=750 °C**	**T=800 °C**
Position 1	0.898	0.898	0.898
Position 2	0.894	0.894	0.894
Position 3	0.893	0.893	0.893
Average	0.895	0.895	0.895
Standard Deviation	0.002	0.002	0.002

Average 0↔25 cycles	0.897	**0.897**	0.897

Table 6 shows the ε_{IR} values at different temperatures, measuring positions and cycle counts for the uncoated sample number 73. The measuring position seems to have a slight impact on the outcome of the calculation since values differ at certain positions. Furthermore, a negligible influence of temperature is opposed by an obvious influence of solar radiation, changing the calculated values between 0 and 25 cycles by up to 4%.

Table 6: ε_{IR} values at different temperatures, measuring positions and cycle counts for uncoated sample number 73

Sample 73 at 0 cycles	**T=700 °C**	**T=750 °C**	**T=800 °C**
Position 1	0.682	0.682	0.682
Position 2	0.669	0.668	0.668
Position 3	0.687	0.687	0.687
Average	0.679	0.679	0.679
Standard Deviation	0.008	0.008	0.008

Sample 73 at 25 cycles	**T=700 °C**	**T=750 °C**	**T=800 °C**
Position 1	0.711	0.711	0.710
Position 2	0.696	0.696	0.696
Position 3	0.716	0.716	0.716
Average	0.708	0.708	0.707
Standard Deviation	0.009	0.009	0.009

Average 0↔25 cycles	0.694	**0.693**	0.693

As mentioned before, the measured spectral raw value of reflection is weighted with the daily FTIR-Baseline and the spectrum of a reference sample. Figure 35 illustrates the results of this procedure for a coated (left, number 89) and an uncoated sample (right, number 73). The roughly constant raw value of reflectance (0.18) for the coated surface is getting attenuated continuously until a wavelength of about $8.1\ \mu m$. For wavelengths of above $8.1\ \mu m$ the weighted values of reflectance are about 13 percentage points lower than the measured raw values.

The uncoated sample possesses a constantly higher measured raw value of reflectance (0.56). The influence of weighting is more significant and also resulting in a continuous attenuation until a wavelength of about $8.1\ \mu m$. For wavelengths of above $8.1\ \mu m$, the aforementioned roughly constant raw value is linked to a weighted value of reflectance that is up to 40 percentage points lower.

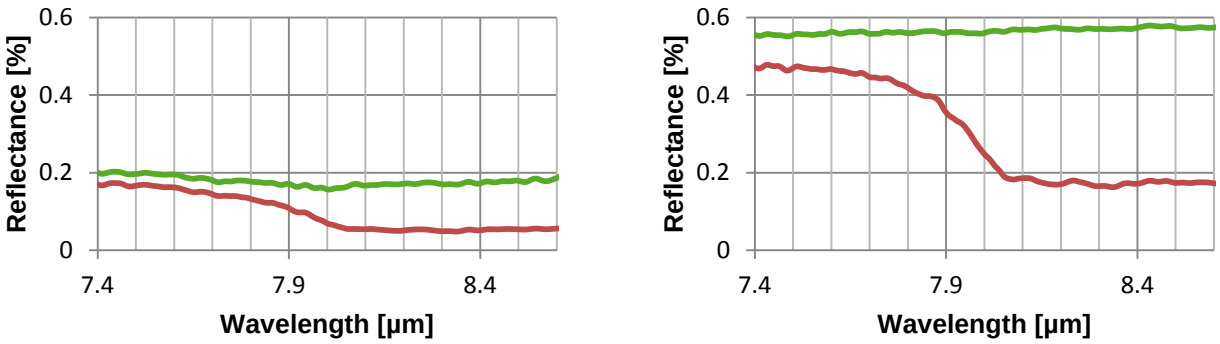

Figure 35: Exemplary illustration of the effect of weighting (red line) the measured raw value of reflectance (blue line) with the daily FTIR-Baseline and a reference sample in the wavelength range of the IR camera for samples 89 (left) and 73 (right)

Figure 36 shows the raw version of the analyzed thermal image. It is taken during the 12th cycle of the dish test procedure. Due to the elevation of the dish system, the sample arrangement appears to be turned by $180\,°$ compared to Figure 10. The coated exemplary sample is indicated with a green circle and the uncoated one with a white circle. The raw, unweighted temperature values with a fixed emittance set equal to 1.00 for all samples can be found in the Appendix. The same applies to the weighted values.

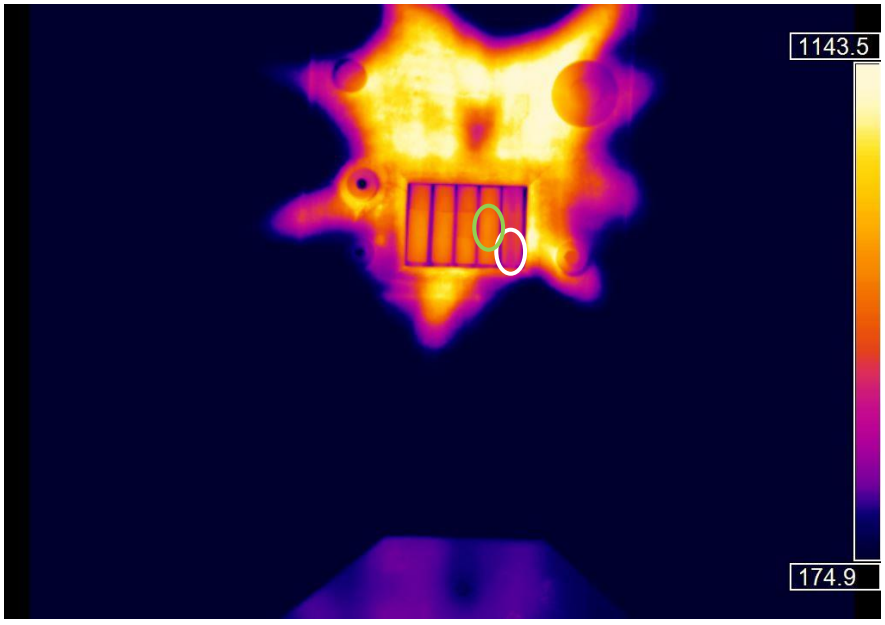

Figure 36: Raw version of the analyzed thermal image (Temperatures displayed at the reference bar are in °C). The Position of the exemplary samples is indicated with a green (coated sample) and a white (uncoated sample) circle.

The raw value of measured temperature of the coated exemplary sample is found out to be $726.4\,°C$. The thermal emittance of the sample in the wavelength range of the IR camera is $\varepsilon_{IR} = 0.897$. The extraction of an IR image with this emittance value leads to a temperature increase (ΔT_{IR}) of $47.6\,°C$ and a weighted surface temperature of $774.1\,°C$. The uncoated sample number 73 possesses a lower raw value of measured temperature ($523.3\,°C$). Nevertheless, the lower thermal emittance value of the sample in the wavelength range of the IR camera ($\varepsilon_{IR} = 0.693$) leads to an increase of weighted temperature by $116.8\,°C$ (see Table 7 and Figure 37).

Summarizing the observed results it can be stated, that a high ε_{IR} value results in a smaller value of correction and vice versa. This also applies for the rest of the considered samples. Coated samples, all with ε_{IR} values above 0.88 show an average value of correction equal to $45.8\,°C$. Whereas uncoated samples with ε_{IR} values between 0.69 and 0.71 show an average value of correction equal to $113\,°C$.

Table 7: Temperature change through weighting of the raw values with specific ε_{IR}

Sample Number	Raw value of measured temperature ($T_{IR,raw}$, with ε_{IR} = 1) [°C]	Weighted temperature ($T_{final,TMS2}$) [°C]	ΔT_{IR} [°C]
89	726.4	774.1	47.6
73	523.3	640.2	116.8

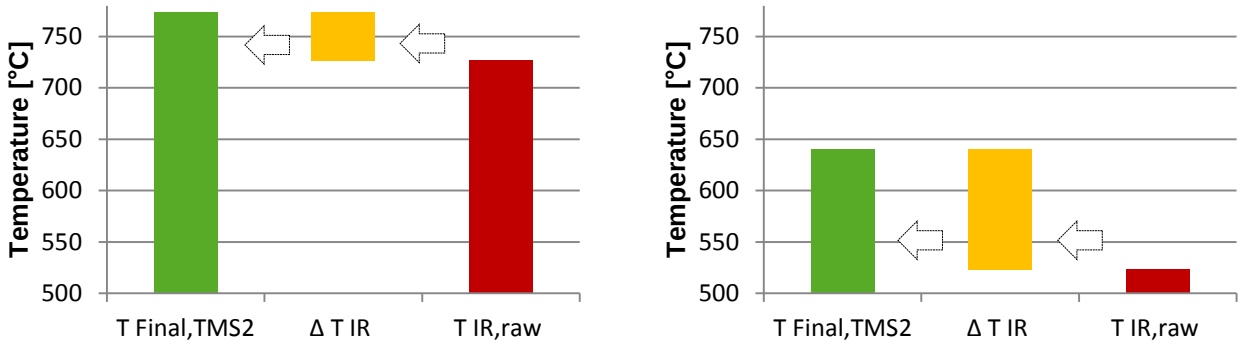

Figure 37: Temperature assessment using TMS 2 for exemplary samples number 89 (left, coated) and 73 (right, uncoated)

5.3 Comparison of TMS 1 and TMS 2

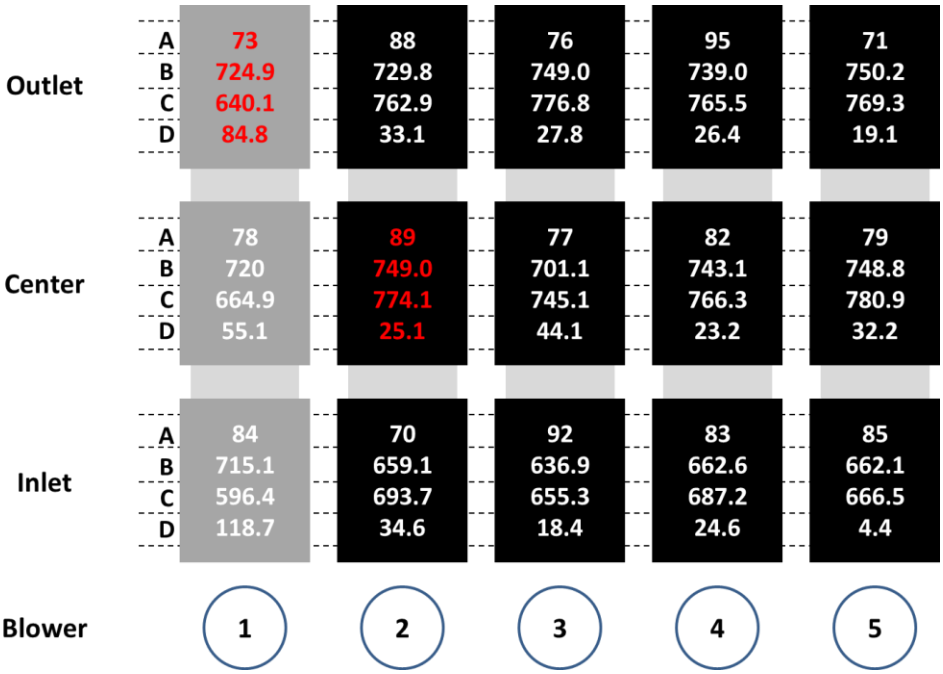

Figure 38: Comparison of temperature values for each sample number (A), derived from both temperature measurement systems. TMS 1 (B), TMS 2 (C) and temperature difference (D). All temperatures are in °C, exemplary samples are indicated in red.

The outcome of the application of both TMS is graphically illustrated in Figure 38. For each sample number (A), the surface temperature derived from TMS 1 (B) and TMS 2 (C) is depicted. Furthermore, the difference in temperature is shown (D).

Surface temperatures of coated samples range from $636.9\,°C$ (sample 92, TMS 1) to $780.9\,°C$ (sample 79, TMS 2). Samples positioned at the inlet of the cooling airflow possess colder surface temperatures than samples positioned at the center and at the outlet. Average values for coated samples are $710.9\,°C$ (TMS 1) and $737\,°C$ (TMS 2). Standard deviations are $43.7\,°C$ (TMS 1) and $47.1\,°C$ (TMS 2).

For each coated sample, the temperature derived from TMS 2 is higher than the temperature derived from TMS 1. The average difference is $26.1\,°C$, the standard deviation is $9.9\,°C$. With a difference of $25.1\,°C$, the selected coated exemplary sample (89) is representative for the respective group, as well as samples 76, 83, 82, 95 (String 4).

For the uncoated samples, temperatures derived from both measurement systems range from $377.4\,°C$ (sample 78, TMS 1) to $742.9\,°C$ (sample 73, TMS 1). The fluctuations in calculated values are higher at this point. Average temperatures derived from both measurement systems are

$605.1\,°C$ (TMS 1) and $633.8\,°C$ (TMS 2). The average value of difference between the two systems is $163°\,C$ with a higher standard deviation of 88.7.

For both exemplary samples, the corrections of the raw values and the outcome of surface temperature depending on the use of the respective measurement system is compared graphically in Figure 39 and Figure 40. For the coated sample number 89, the final temperature derived from TMS 1 is lower than the final temperature derived from TMS 2.

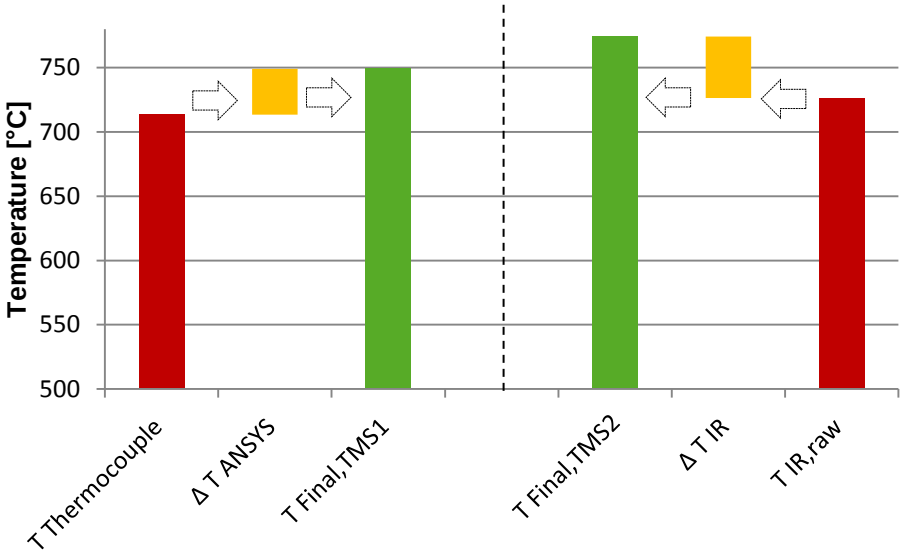

Figure 39: Comparison of temperature derivation from both temperature measurement systems for coated sample number 89

The temperature derivation for the uncoated exemplary sample number 73 shows complementary results. The Final temperature for this sample using TMS 1 is higher than the resulting temperature using TMS 2 for derivation. Whilst the calculated ΔT_{ANSYS} value is also lower than the calculated ΔT_{IR} value, the initial thermocouple temperature is higher than the raw IR image value.

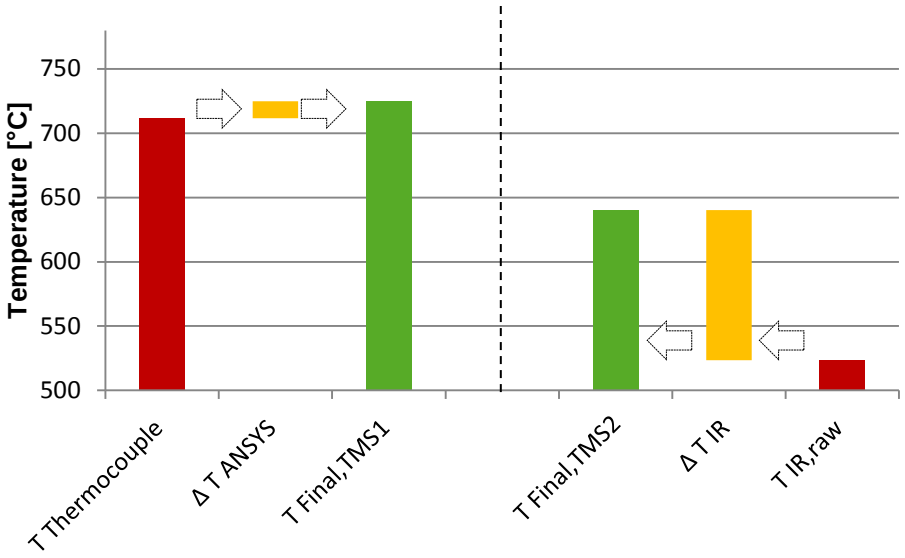

Figure 40: Comparison of temperature derivation from both temperature measurement systems for coated sample number 73

6. Discussion

In the following, possible influences and weaknesses of the deployed systems are discussed. Furthermore, the sensitivity of values to changes under the respective circumstances is examined. As in the same way in the previous chapter, the examination is focused on the two exemplary samples and more information is to be found in the Appendix for other samples.

6.1 TMS 1

The existent procedure to calculate a control point for the thermocouple temperature in the automated dish operating software is derived from the aforementioned simple analytical tool for thermal conduction of a flat, coated sample. Applying the tool, it can be found out that a targeted skin temperature (setpoint) of $750° C$ leads to a thermocouple temperature of $710\,°C$, whereupon $30° C$ of heat losses are calculated and a tolerance of $10\,°C$ is added.

In Figure 41, the results of deviation calculation from the ANSYS simulation are compared to those of the simple analytical tool for a flat and a tubular geometry. The depicted exemplary results are representative for the particular application of calculation method (Tool (flat), Tool (tubular), ANSYS simulation) and sample group (coated, uncoated). The average value of deviation for coated samples derived from the tubular tool model is $23.3\,°C$. The same value derived from the flat tool model is $27.2\,°C$, whilst the value derived from ANSYS is $36.1\,°C$. The same order applies for the uncoated samples. The derivation derived from the tubular tool model is $3.6\,°C$, whilst the derivation from the flat tool model is $7\,°C$ and the one from ANSYS is $16.7\,°C$.

Summarizing the observed results it can be stated, that for the two sample groups and all three types of tools, fluctuations are in the range of $13\,°C$. With the respective tolerance of $10\,°C$ that is added in the existing calculation progress, the results of the established procedure can be confirmed within a few $°C$ for coated and uncoated samples.

Nevertheless, during the ANSYS simulation several parameters are still neglected. An implementation of terms of convection towards the ambient and thermal radiation exchange between the hot sample surfaces themselves and with the ceramic protection around could further impact the simulation. During the conduct of simulation, the three-dimensional tubular geometry is separated into smaller parts. This process is called meshing. A finer mesh and thus a more precise calculation could be conceivable as well in order to achieve more reliable results.

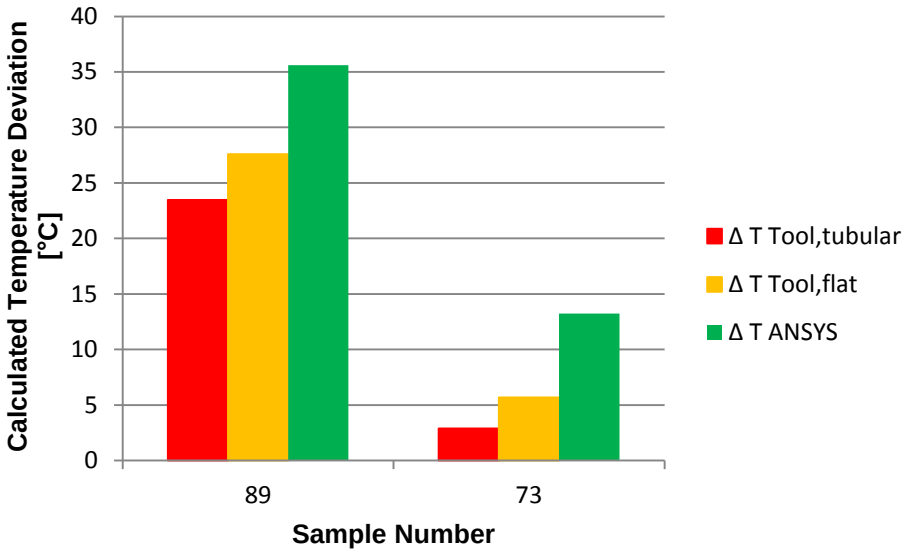

Figure 41: Comparison of different approaches to calculate temperature deviation between thermocouple and sample surface depicted for a coated (number 89) and an uncoated (number 73) sample

6.2 TMS 2

The correct initial default calibration of the IR camera itself at a small distance ($1\ m$) is confirmed in the laboratory beforehand using a blackbody radiation source. Furthermore, the assessment of solar blindness reveals that only a negligible amount of solar radiation has an influence on the measured results. Possible measurement errors due to the weighting of the IR camera images (with the corresponding ε_{IR} values for each sample) are analyzed in the following to identify the systems' sensitivity with respect to ε_{IR}.

In Figure 44, temperatures derived from the IR image section of the coated sample number 89 with various fixed ε_{IR} emittance values along the measured values for solar absorptance and thermal emittance are displayed. The ε_{IR} emittance value that has been determined beforehand is 0.897 and leads to a surface temperature of $774.1\ °C$. The temperature derived with a fixed ε_{IR} emittance of 0.85 turns out to be $799.1\ °C$, whereas the temperature derived with a fixed ε_{IR} emittance of 0.9 turns out to be $772.6\ °C$. With the present measured values, a trendline can be determined, that is displayed in the figure as well. Considering the equation of the trendline in the range of the predetermined ε_{IR} value, it can be stated that a $1\ \%$ increase of the ε_{IR} value leads to a decrease of measured temperature by $4.5\ °C$ $(0.58\ \%)$ and vice versa. With this approach, the sensitivity of measured temperature to changes in the ε_{IR} value can be quantified.

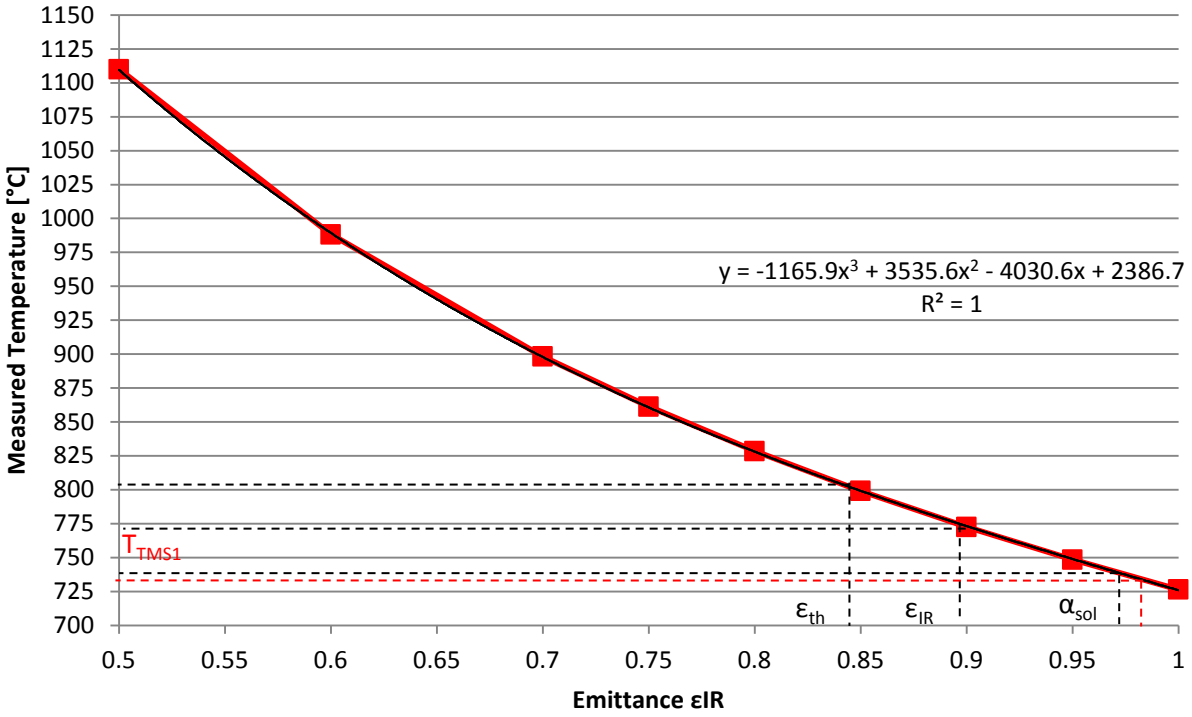

Figure 42: Temperatures derived from the IR image section of the coated sample number 89 with various fixed ε_{IR} emittance values

According to the aforementioned approach, a similar sensitivity examination is conducted for the uncoated exemplary sample. Temperatures derived from the IR image section of sample number 73 with various fixed ε_{IR} emittance values along the measured values for solar absorptance and thermal emittance are displayed in Figure 43. The ε_{IR} emittance value that has been determined beforehand is 0.693 and leads to a surface temperature of $640.2\,°C$. The temperature derived with a fixed ε_{IR} emittance of 0.7 turns out to be $636.6\,°C$, whereas the temperature derived with a fixed ε_{IR} emittance of 0.6 turns out to be $694.7\,°C$. Furthermore, a $1\,\%$ increase of the ε_{IR} value leads to a decrease of measured temperature by $3.6\,°C$ ($0.56\,\%$) and a $1\,\%$ decrease of the ε_{IR} value leads to an increase of measured temperature by $3.7\,°C$ ($0.57\,\%$).

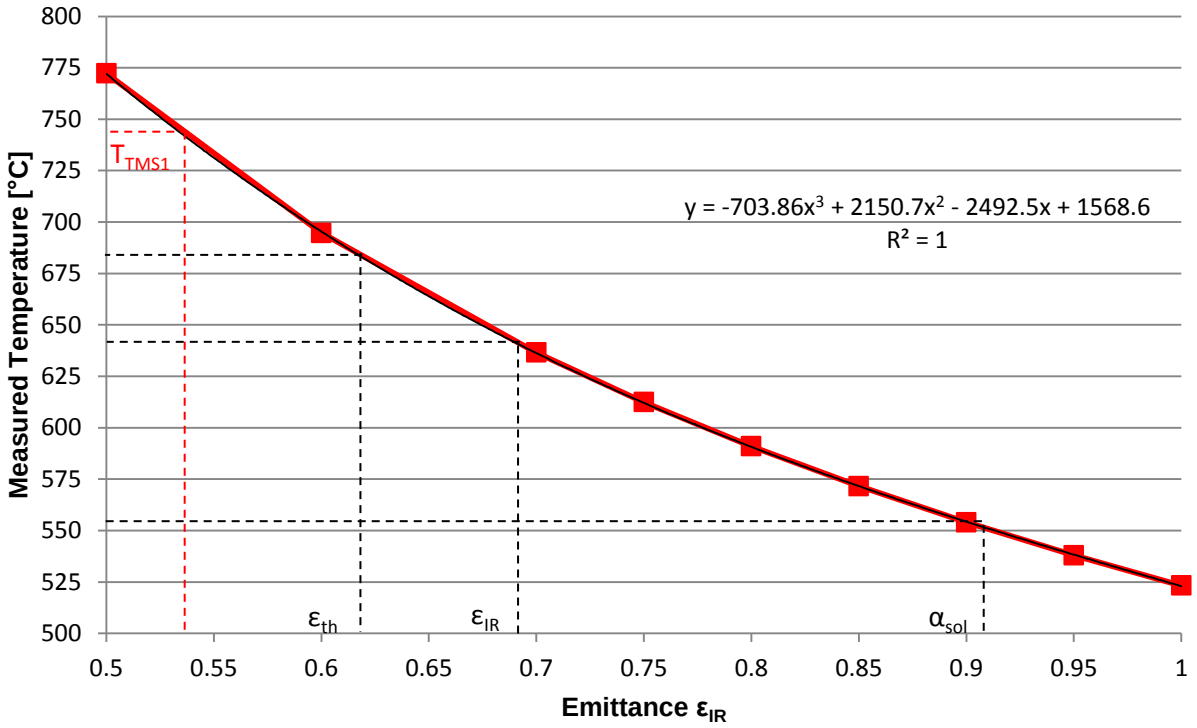

Figure 43: Temperatures derived from the IR image section of the coated sample number 73 with various fixed ε_{IR} emittance values

Regarding the fact that a variation of ε_{IR}values leads to significant temperature differences the FTIR measurements, where ε_{IR} values are derived from can be a source of errors. Devices of this type have a certain measurement uncertainty of $\pm$ 2%. Furthermore, measurements are conducted at room temperature. The elevated temperature setpoint of the dish has an influence only in the weighting of the measured results with the blackbody spectrum. Also the geometry of the tubular samples might have a certain influence as FTIR measurements are usually carried out on plane surfaces.

As described in chapter 4.2.4, a decrease of measured temperature with increasing measurement distance is detected for the blackbody radiation source in the laboratory. Moreover a decrease of measurement temperature with decreasing size of the measured object is noticed. At this point, these effects are not taken into account and could be subject to further investigation.

6.3 Comparison of TMS 1 and TMS 2

For an improvement of the entire temperature measurement at the dish test facility, the two systems have to be comparable and reliable. In Figure 44 a horizontal line of present temperatures along the edge of the coated exemplary surface of the sample is created using both measurement systems. The ANSYS simulation provides a finer resolution than the IR camera image, with some

noise due to meshing, whereas the line provided by the IR camera consists of only 17 values with little recognizable scattering. As described before, the values derived from TMS 2 are around $30\,°C$ higher than those derived from TMS 1.

A reason for scattering of the ANSYS values could be the coarse meshing mentioned above. Furthermore at a measuring distance of $5\,m$, one pixel of the IR image represents a width of $2.05\,mm$ of the measured object, resulting in an overall amount of 16 to 17 pixels to show a horizontal line along the surface of a sample. Compared to the overall size of the IR image ($640\,x\,480$), this is only a very small amount. As a possible reason, the depicted line of IR image values does not seem to be perfectly centered and symmetrical.

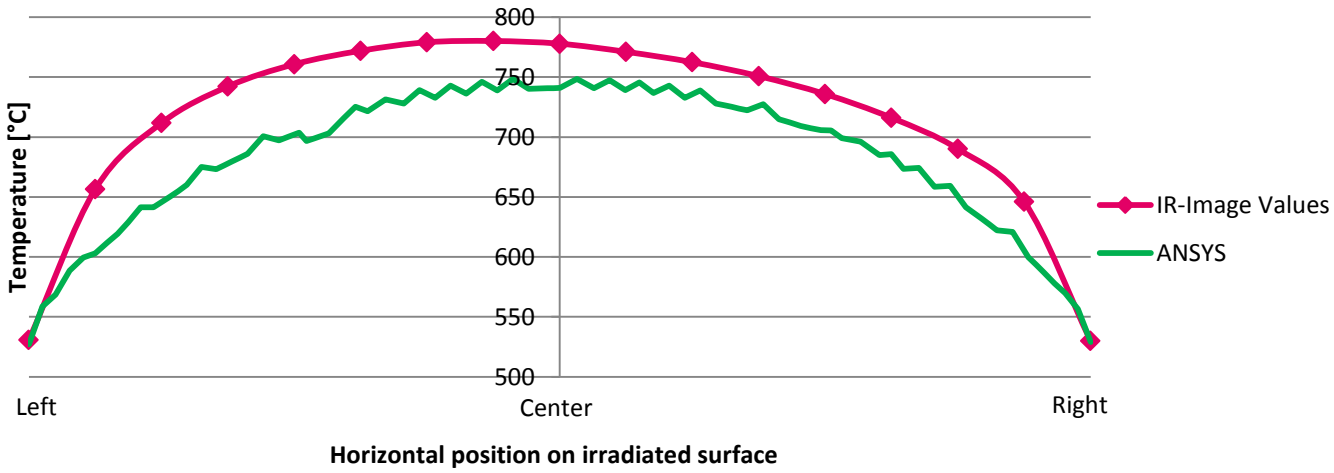

Figure 44: Temperature values of a horizontal line along the surface for coated sample number 89 comparing both introduced measurement systems

According to Figure 44, Figure 45 shows temperature values of a horizontal line along the surface of the uncoated exemplary sample derived from both measurement systems. The line derived from TMS 1 seems to be smoother under these circumstances and the line derived from TMS 2 shows irregularities and again asymmetry.

Due to the omitting of the ceramic coating layer, the ANSYS simulation possibly possesses more precise output values. The ceramic coating layer on top of the substrate material is very thin with a fixed thermal conductivity, whereas the uncoated substrate material is simulated with temperature dependent thermal conductivities throughout the whole volume of the considered geometry. Moreover, due to the inconsistent emittance values in the wavelength range of the camera at different measurement positions (see Table 6), the IR image could appear as not being representative for a sample with an uncoated surface.

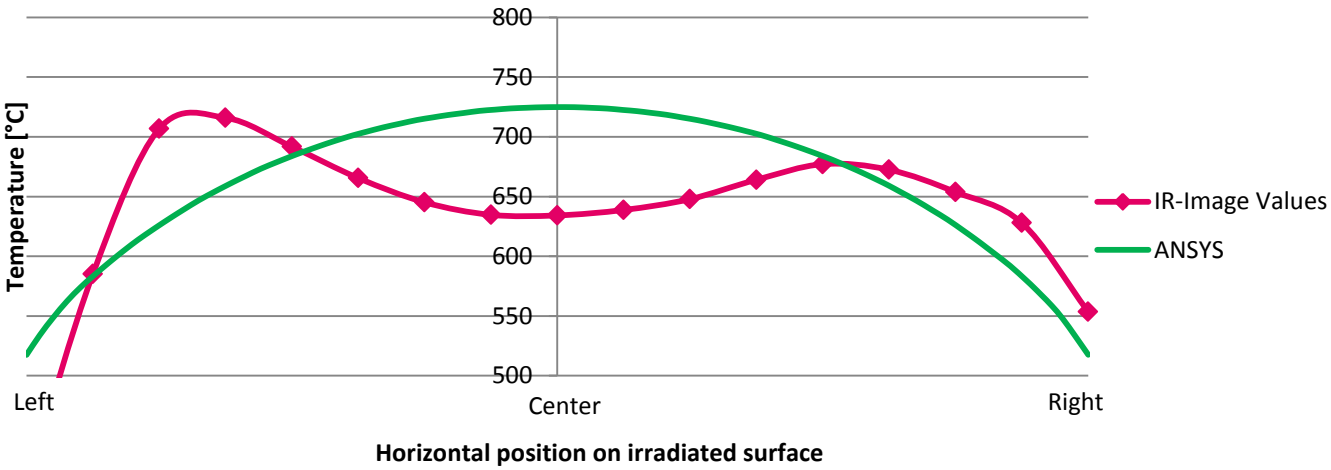

Figure 45: Temperature values of a horizontal line along the surface for coated sample number 73 comparing both introduced measurement systems

This notion is supported by the evidence provided in Figure 46. Pictures taken of the uncoated sample before thermal cycling tests and after 25 cycles show that due to the thermal irradiation, the surface appearance changes and optical degradation is visible. This might also affect the measurement and the reliability of ε_{IR} values. With the approach that is carried out, the exact ε_{IR} value of the sample surface during the cycling tests cannot be determined precise enough to be matched to the point in time where the IR image is taken. This is a source of error and could be subject to further investigation.

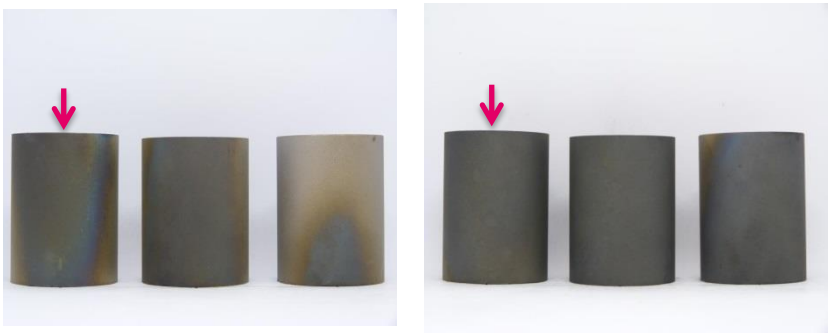

Figure 46: Pictures taken from uncoated samples positioned in line one. After the solar curing procedure and before cycling tests (left) and after 25 cycles (right). Sample number 73 is indicated with a red arrow.

For the coated exemplary sample (see Figure 47), no significant change of surface properties and no optical degradation is visible. Coated samples seem to be more resistant towards thermal irradiation than uncoated ones, resulting in more consistent ε_{IR} values (see Table 5). Therefore, the

applicability of TMS 2 to coated samples with consistent ε_{IR} values and little optical degradation can be confirmed.

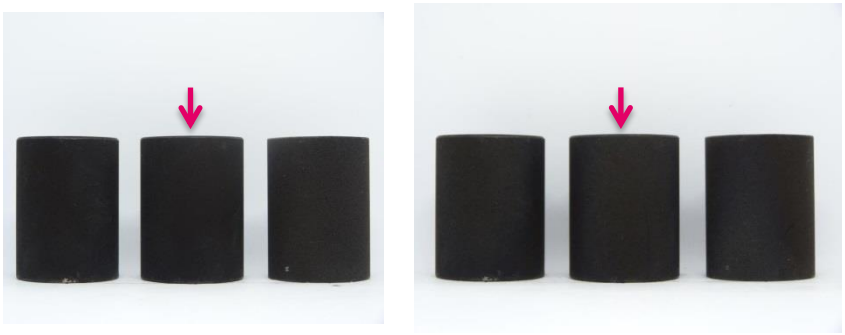

Figure 47: : Pictures taken from coated samples positioned in line two. After the solar curing procedure and before cycling tests (left) and after 25 cycles (right). Sample number 89 is indicated with a red arrow.

7. Summary and Outlook

In the scope of the practical work, the existing temperature measurement system for the dish test bench is enhanced by a simulation using *ANSYS Thermal* (TMS 1). A 3D model of the sample geometry is created and the present heat flows are simulated. Geometric parameters, optical parameters and the thermocouple temperature measured during the test are taken into account to derive the present surface temperature of the examined samples. The average surface temperature is $711.2\,°C$ for coated and $605.7\,°C$ for uncoated samples, the average difference between thermocouple and skin temperature is $35.9\,°C$ for coated and $20.1\,°C$ for uncoated samples. Thus, the applicability of the existing tool for a temperature setpoint calculation at the dish test bench can be confirmed within a few °C.

After the conduction of experiments regarding calibration, a new temperature measurement system using a solar blind infrared camera is implemented (TMS 2). Therefore, the specific thermal emittance in the wavelength range of the IR camera is derived from results of the optical sample characterization routine of dish cycling test procedure. The raw IR image is then weighted with the specific values for each sample to create a refined and differentiated overview of sample surface temperatures. Coated samples on the one hand, show a thermal emittance (ε_{IR}) that is constant over various cycles, measurement positions and temperatures of the blackbody spectra in the relevant range. Uncoated samples on the other hand, show susceptibility towards solar radiation. This is manifested in fluctuating values at different measuring positions and cycles and is also visually recognizable. Average surface temperatures derived from TMS 2 are $737\,°C$ for coated and $633.8\,°C$ for uncoated samples, the average difference between unweighted IR image temperature is $\pm 45.8\,°C$ for coated and $\pm 113\,°C$ for uncoated samples.

In comparison, the average temperature derived from TMS 1 for coated samples is $28.1\,°C$ below the average temperature derived from TMS 2, whereas the average temperature derived from TMS 1 for uncoated samples is $163.7\,°\,C$ above the average temperatures derived from TMS 2.

The improvement of the ANSYS simulation offers some starting points for future research. Additional terms to simulate a more precise heat flow (e.g. the convection from the hot outer surface of the sample towards the ambient) could be taken into consideration. Also the heat radiation exchange between the certain sample surfaces and other sample lines or between sample surfaces and the surroundings (e.g. the ceramic heat protection) could be considered. Moreover, a mesh analysis could be carried out to improve the model precision.

As shown in the previous chapter, the results derived from TMS 2 are sensitive towards the value of ε_{IR}. Therefore, the FTIR measurements can be considered as a source of error. Research to improve the precision and reliability of the FTIR values could include reproducible and standardized measurements on curved surfaces and real measurements at relevant temperatures. Furthermore, the conditions for creating IR images can be improved. Mounting the camera at a position that is closer to the surface of the samples would improve the precision of measured values and the resolution of the samples as they would cover a larger area in the IR image.

During camera calibration test in the laboratory, a decrease in measured temperature with increasing measuring distance and decreasing object size is discovered. The latter could indicate a susceptibility to the so-called “slit-response function” [43]. In the post processing of the raw IR images, the mentioned disturbances could be taken into account in order to improve the weighting process and to derive more precise and reliable temperature values.

8. Bibliography

1. National Institute of Science and Technology (NIST), *The NIST Reference on Constants, Units, and Uncertainty*,2015 ; Available from: https://physics.nist.gov/cuu/Constants/ (Accessed 17.09.2018)

2. Kopp, G. and Lean, J.L., *A new, lower value of total solar irradiance: Evidence and climate significance.* Geophysical Research Letters, 2011. **38**(1)

3. Raiselife Project, 2018 ; Available from: https://www.raiselife.eu/ (Accesed 05.09.2018)

4. Enerdata *Global Energy Statistical Yearbook 2018*. 2018; Available from: https://yearbook.enerdata.net/electricity/electricity-domestic-consumption-data.html (Accesed 28.09.2018)

5. European Comission 2015; Available from: https://ec.europa.eu/clima/policies/international/negotiations/paris_de (Accesed 28.09.2018)

6. Lazard, *Lazard's levelized cost of energy analysis - Version 11.0.* 2017.

7. New Energy Update, *ACWA Power scales up tower-trough design to set record-low CSP price*. 2017; Available from: http://newenergyupdate.com/csp-today/acwa-power-scales-tower-trough-design-set-record-low-csp-price. (Accesed 28.09.2018)

8. DLR, *Aerial Image of the PSA*; Available from: https://www.dlr.de/Portaldata/1/Resources/portal_news/newsarchiv2006/kooperation_solar_130606/plataforma_solar_almeria.JPG. (Accesed 05.09.2018)

9. Heller, P., *The performance of concentrated solar power (CSP) systems*. 2017

10. Ragheb, M., *Solar Thermal Power and Energy Storage Historical Perspective.* 2014

11. Pitz-Paal, R., University Lecture "Solar Technology", 2014: Institute of Solar Research, RWTH Aachen

12. National Renewable Energy Laboratory of the United States; Available from: https://www.nrel.gov/csp/solarpaces/project_detail.cfm/projectID=44 (Accesed 05.09.2018)

13. Solargis, Solar Resource Map - Direct Normal Irradiation, 2018.

14. Hoffschmidt, B. and Alexopoulos, S. *Überblick über solarthermische Kraftwerke* DPG AKE-Tagungsband, 2009.

15. Office of Energy Efficiency & Renewable Energy (U.S. Department of Energy), *Concentrating Solar Power Basics*. 2013; Available from: https://energy.gov/eere/energybasics/articles/concentrating-solar-power-basics (Accesed 28.09.2018)

16. Plumpe, A., *Design of a Test Rig and its Testing Methods for Rotation and Expansion Performing Assemblies in Parabolic Trough Collector Power Plants*, 2016.

17. Sunwindenergy.com, *Image of a PTC power plant in operation*. Available from: http://www.sunwindenergy.com/sites/default/files/news/solar%20trough%20photo%20credit%20gossamer%20%282%29.jpg (Accesed 05.09.2018)

18. Elsevier B.V., *Progress in concentrated solar power technology with parabolic trough collector system*, 2017. Available from: https://ars.elscdn.com/content/image/1-s2.0-S1364032117308122-gr2.jpg (Accesed 05.09.2018)

19. Federal Ministry for Environment, Nature Conservation and Nuclear Safety (BMU), *Solar Thermal Power Plants - Utilising concentrated sunlight for generating energy*, 2013.

20. Geyer, M. et al., *Solarthermische Kraftwerke - Technologie und Perspektiven*, in *Jahrestagung des Forschungsverbunds Sonnenenergie* 2002.

21. STELA World, *Image of a Linear Fresnel power plant in operation*. Available from: http://www.stelaworld.org/wp-content/uploads/2014/Fresnel-Novatec-Solar_Fresnel-Boiler-1024x767.jpg (Accesed 05.09.2018)

22. Roldán Serrano, M.I., *Concentrating Solar Thermal Technologies* **88**: p.25

23. Ho, C.K., *Advances in central receivers for concentrating solar applications.* Solar Energy, 2017. **152**: p. 38-56.

24. Finetubes, *Solar Tower power plant in operation*. Available from: http://www.finetubes.de/uploads/images/gemasolar-2011-2_low_res..jpg (Accesed 05.09.2018)

25. Australian Academy of Science, *Image of an operating Solar Dish facility*. Available from: https://www.science.org.au/curious/technology-future/concentrating-solar-thermal (Accesed 10.09.2018)

26. Ho, C.K., Mahoney, A.R. and Ambrosini, A. *Characterization of Pyromark 2500 Paint for High-Temperature Solar Receivers* 2013: ASME International

27. Ho, C.K. and J.E. Pacheco, *Levelized Cost of Coating (LCOC) for selective absorber materials.* Solar Energy, 2014. **108**: p. 315-321.

28. Hildebrandt, C., *Selective Absorbers for Solar Thermal Power Plants*, in *RAISELIFE Dissemination Workshop* 2017.

29. Caron, S., et al., *Accelerated Ageing of Solar Reciever Coatings: Experimental Results for T91 and VM12 Steel Substrates* 2017.

30. Marzo, A., et al., *Solar blind pyrometry not relying on atmospheric absorption bands.* Solar Energy, 2014. **107**: p. 415-422.

31. Pfänder, M., *Pyrometrische Temperaturmessung an solarthermischen Hochtemperaturreceivern*, 2006, TU Bergakademie Freiberg.

32. Laing, D.e.a., *Dish-Stirling-Systeme - Eine Technologie zur dezentralen solaren Stromerzeugung.* FVS Themen, 2002.

33. ANSYS, *Exported Image of the conducted ANSYS simulation during the test campaign*, 2018.

34. VDI,*VDI Heat Atlas*2010; Springer Berlin Heidelberg

35. Vollmer, M. and K.-P. Möllmann, *Infrared thermal imaging* 2018

36. Pfeifer, H., *Transportphänomene 1*, 2013: RWTH Aachen Lecture Manuscript

37. Sun.org, *Black-body spectrum*, 2017.

38. Israel, M., *Entwicklung eines UAV-basierten Systems zur Rehkitzsuche und Methoden zur Detektion und Georeferenzierung von Rehkitzen in Thermalbildern*, 2016, Universität Osnabrück.

39. Prante, N., *Radiometric chain of camera mounted at dish facility*, 2018.

40. Optris Infrared Thermometers, *Operators Manual optris® PI 160/ 200/ 230/ 400/ 450/ 450 G7/ 640/ 640 G7/ 1M*, 2017.

41. ASTM, *Standard Solar Constant and Zero Air Mass Solar Spectral Irradiance Tables*, 2014.

42. Spectral Sciences Incorporated. *Modtran*. 2018; Available from: http://modtran.spectral.com/ (Accessed on: 13.09.2018)

43. Riou, O., Félix Durastanti, J. and Tortel, V. *Evaluation of error in temperature starting from the Slit Response function and calibration curve of a thermal focal plane array camera* 2006.

44. Independent Wholesale Welding Supply, *Datasheet Pyromark 2500* , Available from: https://www.iwws.net/files//msds_forms/pyromark_2500_flat_black.pdf (Accessed on: 24.09.2018)

45. Special Metals, *Inconel alloy 617*, 2005. Available from: http://www.specialmetals.com/assets/smc/documents/alloys/inconel/inconel-alloy-617.pdf (Accessed on: 24.09.2018)

46. Haynes Intl.., *Haynes 230 Alloy Principle Features*, 2018. Available from: http://haynesintl.com/docs/default-source/pdfs/new-alloy-brochures/high-temperature-alloys/brochures/230-brochure.pdf (Accessed on: 24.09.2018)

9. List of figures

10. List of tables

11. Appendix

11.1 Datasheets

9. Physical and Chemical Properties

Physical state : Black Liquid Paint
Feezing Point: Not Determined
Odour : aromatic Naphtha odour
pH value : Not determined
Vapour Density [Air=1]: 3.8
Vapour Pressure: 2.5 mmHg

Solubility in water : Negligable
Boiling Point: 110-193°C (230-380°F)
% Volatiles by Volume: 50% Approx
Flash point [°C] : 31°C (88°F).
Specific Gravity (Water =1): 1.15
Volatile Organic Compounds (VOC): Typically 624 gms/ltr or 5.2 lbs/gal

Other Properties
None relevant to product.

Figure 48: Excerpt from Datasheet Pyromark 2500 [44]

Table 3 - Electrical and Thermal Properties

Temperature	Electrical Resistivity	Thermal Conductivity[a]	Coefficient of Expansion[b]	Specific Heat[c]
°F	ohm-circ mil/ft	Btu-in./ft²-h-°F	10^{-6} in./in./°F	Btu/lb-°F
78	736	94	-	0.100
200	748	101	7.0	0.104
400	757	113	7.2	0.111
600	764	125	7.4	0.117
800	770	137	7.6	0.124
1000	779	149	7.7	0.131
1200	793	161	8.0	0.137
1400	807	173	8.4	0.144
1600	803	185	8.7	0.150
1800	824	197	9.0	0.157
2000	-	209	9.2	0.163
°C	µΩ-m	W/m-°C	µm/m-°C	J/kg-°C
20	1.222	13.4	-	419
100	1.245	14.7	11.6	440
200	1.258	16.3	12.6	465
300	1.268	17.7	13.1	490
400	1.278	19.3	13.6	515
500	1.290	20.9	13.9	536
600	1.308	22.5	14.0	561
700	1.332	23.9	14.8	586
800	1.342	25.5	15.4	611
900	1.338	27.1	15.8	636
1000	1.378	28.7	16.3	662

[a]Calculated from electrical resistivity.
[b]Mean coefficient of linear expansion between 78°F (26°C) and temperature shown.
[c]Calculated values.

Table 4 - Modulus of Elasticity[a]

Temperature	Tensile Modulus	Shear Modulus	Poisson's Ratio[b]
°F	10^3 ksi	10^3 ksi	
74	30.6	11.8	0.30
200	30.0	11.6	0.30
400	29.0	11.2	0.30
600	28.0	10.8	0.30
800	26.9	10.4	0.30
1000	25.8	9.9	0.30
1200	24.6	9.5	0.30
1400	23.3	9.0	0.30
1600	21.9	8.4	0.30
1800	20.5	7.8	0.31
2000	18.8	7.1	0.32
°C	GPa	GPa	Poisson's Ratio[b]
25	211	81	0.30
100	206	80	0.30
200	201	77	0.30
300	194	75	0.30
400	188	72	0.30
500	181	70	0.30
600	173	66	0.30
700	166	64	0.30
800	157	61	0.30
900	149	57	0.30
1000	139	53	0.31
1100	129	49	0.32

[a]Determined by dynamic method.
[b]Calculated from moduli of elasticity.

Figure 49: Excerpt from Datasheet Inconel617 (1 of 2) [45]

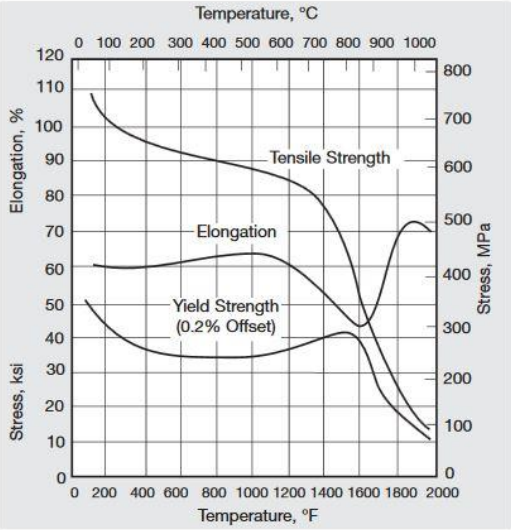

Figure 1. High-temperature tensile properties of solution-annealed, hot-rolled rod.

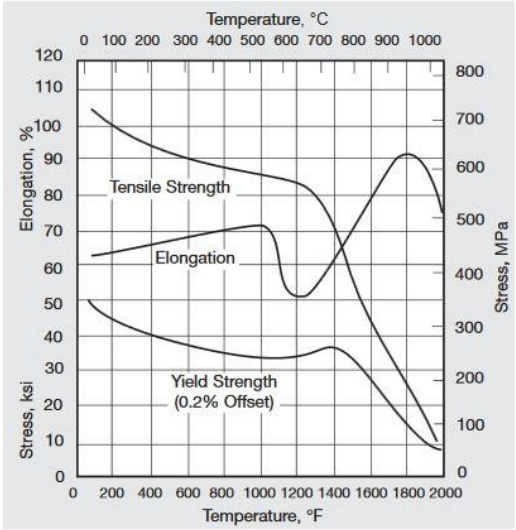

Figure 2. High-temperature tensile properties of solution-annealed, cold-rolled sheet.

Table 5 - Typical Room-Temperature Mechanical Properties of Solution-Annealed Material

Product Form	Production Method	Yield Strength (0.2% Offset)		Tensile Strength		Elongation, %	Reduction of Area, %	Hardness BHN
		ksi	MPa	ksi	MPa			
Plate	Hot Rolling	46.7	322	106.5	734	62	56	172
Bar	Hot Rolling	46.1	318	111.5	769	56	50	181
Tubing	Cold Drawing	55.6	383	110.0	758	56	-	193
Sheet or Strip	Cold Rolling	50.9	351	109.5	755	58	-	173

Figure 50: Excerpt from Datasheet Inconel617 (2 of 2) [45]

Tensile Properties of 230® Sheet

Test Temperature		0.2 % Yield Strength		Ultimate Tensile Strength		Elongation
°F	°C	ksi	MPa	ksi	MPa	%
70	21	60.4	417	121.4	837	47.3
1000	538	42.6	294	100.1	690	51.7
1200	649	42.2	291	96.6	666	56.9
1400	760	45.1	311	78.0	538	59.5
1600	871	34.2	236	44.6	308	74.2
1800	982	17.8	123	24.5	169	54.1
2000	1093	10.0	69	13.1	90	37.0

Tensile Properties of 230® Plate

Test Temperature		0.2% Yield Strength		Ultimate Tensile Strength		Elongation
°F	°C	ksi	MPa	ksi	MPa	%
70	21	55.5	383	123.6	852	46.0
1000	538	38.1	263	102.5	706	53.2
1200	649	38.7	267	98.2	677	53.0
1400	760	37.7	260	77.2	533	68.0
1600	871	33.9	234	45.1	311	94.0
1800	982	16.8	116	24.3	168	91.2
2000	1093	9.1	63	13.2	91	92.1

Figure 51: Excerpt Datasheet Haynes230 (1 of 4) [46]

Physical Property	British Units		Metric Units	
Density	RT	0.324 lb/in³	RT	8.97 g/cm³
Melting Temperature	2375-2500°F	-	1301-1371°C	-
Electrical Resistivity	RT	49.2 µohm-in	RT°C	125.0 µohm-m
	200°F	49.5 µohm-in	100°C	125.8 µohm-m
	400°F	49.8 µohm-in	200°C	126.5 µohm-m
	600°F	50.2 µohm-in	300°C	127.3 µohm-m
	800°F	50.7 µohm-in	400°C	128.4 µohm-m
	1000°F	51.5 µohm-in	500°C	130.2 µohm-m
	1200°F	51.6 µohm-in	600°C	131.2 µohm-m
	1400°F	51.1 µohm-in	700°C	130.7 µohm-m
	1600°F	50.3 µohm-in	800°C	129.1 µohm-m
	1800°F	49.3 µohm-in	900°C	127.1 µohm-m
	-	-	1000°C	125.0 µohm-m
Thermal Diffusivity	RT	3.8 x 10^{-3}in²/sec	RT	24.2 x 10^{-3}cm²/s
	200°F	4.1 x 10^{-3}in²/sec	100°C	26.8 x 10^{-3}cm²/s
	400°F	4.7 x 10^{-3}in²/sec	200°C	29.9 x 10^{-3}cm²/s
	600°F	5.2 x 10^{-3}in²/sec	300°C	32.9 x 10^{-3}cm²/s
	800°F	5.6 x 10^{-3}in²/sec	400°C	35.7 x 10^{-3}cm²/s
	1000°F	6.1 x 10^{-3}in²/sec	500°C	38.5 x 10^{-3}cm²/s
	1200°F	6.5 x 10^{-3}in²/sec	600°C	41.9 x 10^{-3}cm²/s
	1400°F	6.7 x 10^{-3}in²/sec	700°C	43.0 x 10^{-3}cm²/s
	1600°F	6.7 x 10^{-3}in²/sec	800°C	43.2 x 10^{-3}cm²/s
	1800°F	7.3 x 10^{-3}in²/sec	900°C	44.4 x 10^{-3}cm²/s
	-	-	1000°C	48.2 x 10^{-3}cm²/s
Thermal Conductivity	RT	62 Btu-in/ft²-hr-°F	RT	8.9 W/m-°C
	200°F	71 Btu-in/ft²-hr-°F	100°C	10.4 W/m-°C
	400°F	87 Btu-in/ft²-hr-°F	200°C	12.4 W/m-°C
	600°F	102 Btu-in/ft²-hr-°F	300°C	14.4 W/m-°C
	800°F	118 Btu-in/ft²-hr-°F	400°C	16.4 W/m-°C
	1000°F	133 Btu-in/ft²-hr-°F	500°C	18.4 W/m-°C
	1200°F	148 Btu-in/ft²-hr-°F	600°C	20.4 W/m-°C
	1400°F	164 Btu-in/ft²-hr-°F	700°C	22.4 W/m-°C
	1600°F	179 Btu-in/ft²-hr-°F	800°C	24.4 W/m-°C
	1800°F	195 Btu-in/ft²-hr-°F	900°C	26.4 W/m-°C
	-	-	1000°C	28.4 W/m-°C

RT= Room Temperature

Figure 52: Excerpt Datasheet Haynes230 (2 of 4) [46]

Physical Property	British Units		Metric Units	
Specific Heat	RT	0.095 Btu/lb-°F	RT	397 J/kg·°C
	200°F	0.099 Btu/lb-°F	100°C	419 J/kg·°C
	400°F	0.104 Btu/lb-°F	200°C	435 J/kg·°C
	600°F	0.108 Btu/lb-°F	300°C	448 J/kg·°C
	800°F	0.112 Btu/lb-°F	400°C	465 J/kg·°C
	1000°F	0.112 Btu/lb-°F	500°C	473 J/kg·°C
	1200°F	0.134 Btu/lb-°F	600°C	486 J/kg·°C
	1400°F	0.140 Btu/lb-°F	700°C	574 J/kg·°C
	1600°F	0.145 Btu/lb-°F	800°C	5595 J/kg·°C
	1800°F	0.147 Btu/lb-°F	900°C	609 J/kg·°C
	-	-	1000°C	617 J/kg·°C
Mean Coefficient of Thermal Expansion	70-200°F	6.5 µin/in -°F	25-100°C	11.8 x 10-6m/m·°C
	70-400°F	6.9 µin/in -°F	25-200°C	12.4 x 10-6m/m·°C
	70-600°F	7.2 µin/in -°F	25-300°C	12.8 x 10-6m/m·°C
	70-800°F	7.4 µin/in -°F	25-400°C	13.2 x 10-6m/m·°C
	70-1000°F	7.6 µin/in -°F	25-500°C	13.6 x 10-6m/m·°C
	70-1200°F	8.0 µin/in -°F	25-600°C	14.1 x 10-6m/m·°C
	70-1400°F	8.3 µin/in -°F	25-700°C	14.7 x 10-6m/m·°C
	70-1600°F	8.6 µin/in -°F	25-800°C	15.2 x 10-6m/m·°C
	70-1800°F	8.9 µin/in -°F	25-900°C	15.7 x 10-6m/m·°C
	-	-	25-1000°C	16.1 x 10-6m/m·°C
Dynamic Modulus of Elasticity	RT	30.3 mpsi	RT	209 GPa
	200°F	30.1mpsi	100°C	207 GPa
	400°F	29.0 mpsi	200°C	200 GPa
	600°F	27.8 mpsi	300°C	193 GPa
	800°F	26.8 mpsi	400°C	186 GPa
	1000°F	25.9 mpsi	500°C	181 GPa
	1200°F	24.9 mpsi	600°C	175 GPa
	1400°F	23.6 mpsi	700°C	168 GPa
	1600°F	22.2 mpsi	800°C	159 GPa
	1800°F	20.7 mpsi	900°C	150 GPa
	2000°F	19.1 mpsi	1000°C	141 GPa

RT= Room Temperature

Figure 53: Excerpt Datasheet Haynes230 (3 of 4) [46]

Physical Property	British Units		Metric units	
Dynamic Shear Modulus	RT	11.5 mpsi	RT	79 GPa
	200°F	11.4 mpsi	100°C	79 GPa
	400°F	11.0 mpsi	200°C	76 Gpa
	600°F	10.5 mpsi	300°C	73 GPa
	800°F	10.1 mpsi	400°C	70 GPa
	1000°F	9.7 mpsi	500°C	67 GPa
	1200°F	9.3 mpsi	600°C	64 GPa
	1400°F	8.8 mpsi	700°C	61 GPa
	1600°F	8.2 mpsi	800°C	57 GPa
	1800°F	7.6 mpsi	900°C	52 GPa
	2000°F	7.0 mpsi	1000°C	48 GPa
Poisson's Ratio	RT	0.31	RT	0.31
	200°F	0.31	100°C	0.31
	400°F	0.32	200°C	0.32
	600°F	0.32	300°C	0.32
	800°F	0.33	400°C	0.33
	1000°F	0.33	500°C	0.33
	1200°F	0.34	600°C	0.34
	1400°F	0.34	700°C	0.34
	1600°F	0.35	800°C	0.34
	1800°F	0.36	900°C	0.35

RT= Room Temperature

Figure 54: Excerpt Datasheet Haynes230 (4 of 4) [46]

11.2 Exemplary reflectance spectra

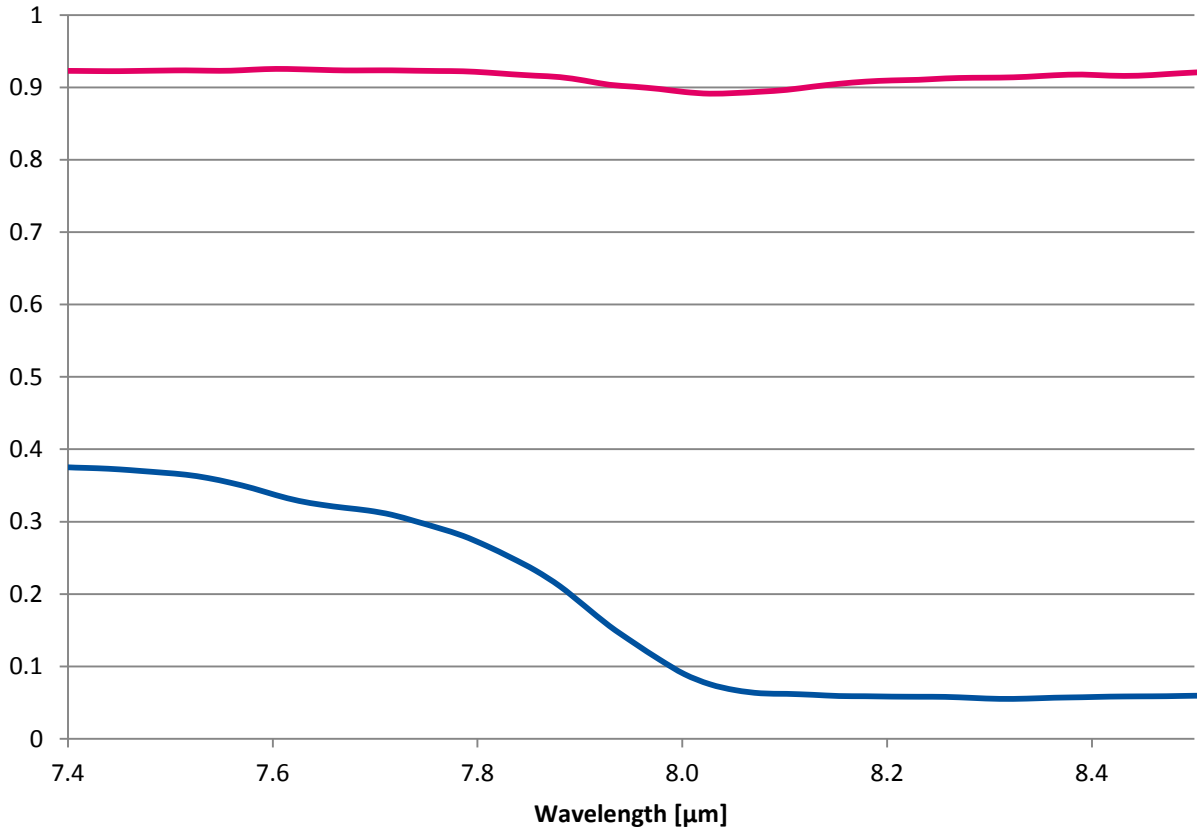

Figure 55: Reflectance spectra in the wavelength range of the Optris IR camera for a black-coated (red line) and a selective coated (blue line) sample

11.3 Experimental Results

11.3.1 Results of camera calibration tests

Temperature set at blackbody	Distance	Diameter of emissive area	Reached Temperature
600°C	1m	16mm	599.8 °C
600°C	1m	14mm	598.8 °C
600°C	1m	12mm	598.2 °C
600°C	1m	10mm	598.4 °C
600°C	1m	8mm	596.3 °C
600°C	1m	6mm	594.9 °C
600°C	1m	4mm	589.9 °C
600°C	3m	16mm	589.3 °C
600°C	3m	14mm	587.2 °C
600°C	3m	12mm	585.5 °C
600°C	3m	10mm	585.3 °C
600°C	3m	8mm	579.1 °C
600°C	3m	6mm	573.4 °C
600°C	3m	4mm	489. °C
600°C	5m	16mm	581. °C
600°C	5m	14mm	575.9 °C
600°C	5m	12mm	572.8 °C
600°C	5m	10mm	570. °C
600°C	5m	8mm	558.1 °C
600°C	5m	6mm	523.5 °C
600°C	5m	4mm	427.4 °C
600°C	1m	16mm	599.8 °C

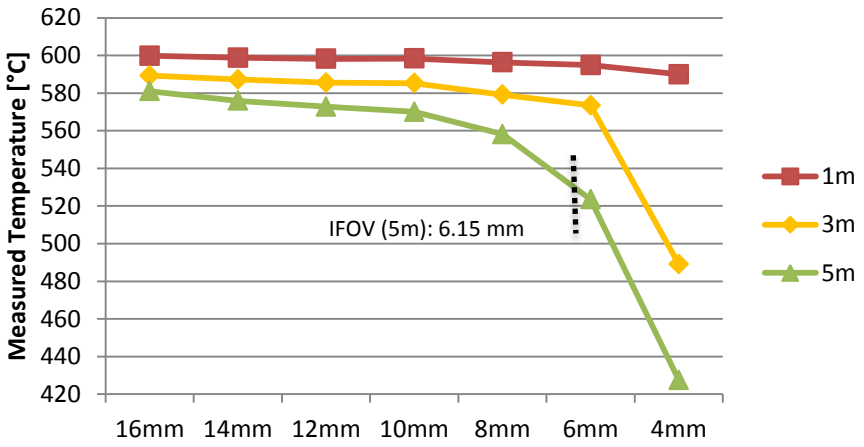

Figure 56: Measured temperatures at different distances and hole diameters (blackbody temperature set to 600°C)

Temperature set at blackbody	Measuring Distance	Diameter of emissive area	Reached Temperature
700°C	1m	16mm	703.5 °C
700°C	1m	14mm	701.4 °C
700°C	1m	12mm	700.6 °C
700°C	1m	10mm	699.3 °C
700°C	1m	8mm	697. °C
700°C	1m	6mm	695.3 °C
700°C	1m	4mm	684.5 °C
700°C	3m	16mm	698.4 °C
700°C	3m	14mm	687.3 °C
700°C	3m	12mm	685.6 °C
700°C	3m	10mm	684.5 °C
700°C	3m	8mm	678.2 °C
700°C	3m	6mm	670.1 °C
700°C	3m	4mm	631.8 °C
700°C	5m	16mm	676.8 °C
700°C	5m	14mm	671.4 °C
700°C	5m	12mm	669.3 °C
700°C	5m	10mm	666. °C
700°C	5m	8mm	651.8 °C
700°C	5m	6mm	585.8 °C
700°C	5m	4mm	393. °C
700°C	1m	16mm	703.5 °C

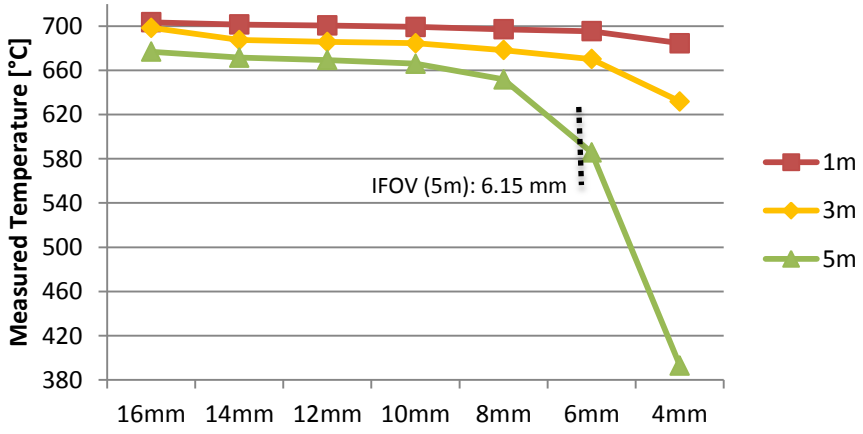

Figure 57: Measured temperatures at different distances and hole diameters (blackbody temperature set to 700°C)

Temperature set at blackbody	Measuring Distance	Diameter of emissive area	Reached Temperature
800°C	1m	16mm	802.4 °C
800°C	1m	14mm	800.8 °C
800°C	1m	12mm	800.5 °C
800°C	1m	10mm	799.6 °C
800°C	1m	8mm	797.5 °C
800°C	1m	6mm	794.1 °C
800°C	1m	4mm	773.1 °C
800°C	3m	16mm	788. °C
800°C	3m	14mm	786. °C
800°C	3m	12mm	784.1 °C
800°C	3m	10mm	783.2 °C
800°C	3m	8mm	775.3 °C
800°C	3m	6mm	765.9 °C
800°C	3m	4mm	730.4 °C
800°C	5m	16mm	776.2 °C
800°C	5m	14mm	770.8 °C
800°C	5m	12mm	766.4 °C
800°C	5m	10mm	763.3 °C
800°C	5m	8mm	750.4 °C
800°C	5m	6mm	710.4 °C
800°C	5m	4mm	537.2 °C
800°C	1m	16mm	802.4 °C

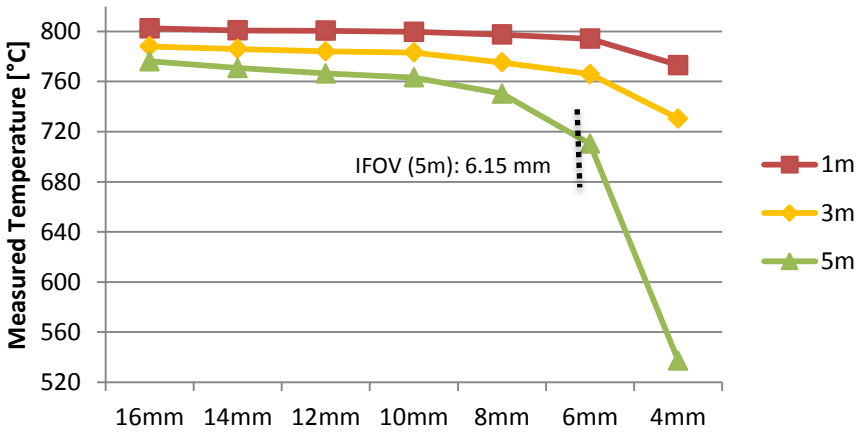

Figure 58: Measured temperatures at different distances and hole diameters (blackbody temperature set to 800°C)

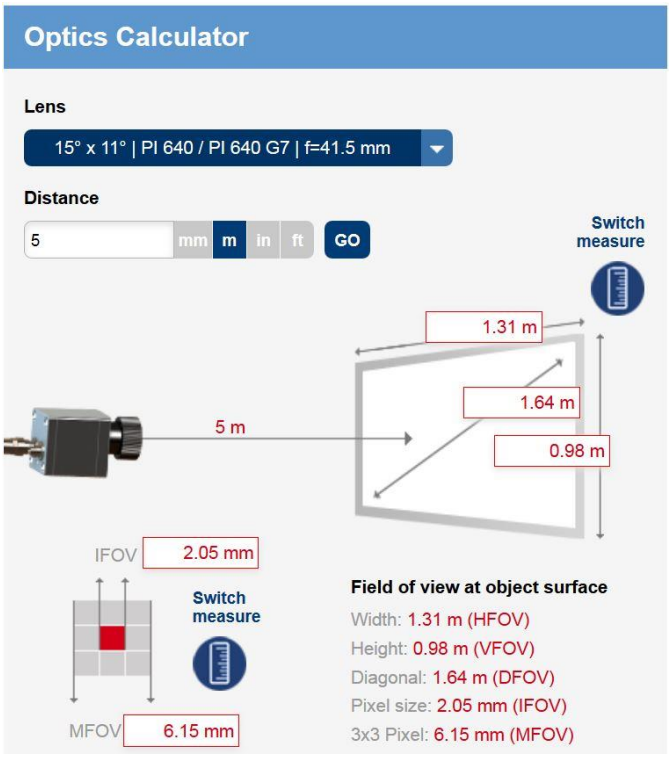

Figure 59: FOV and image size of IR camera with applied optics at measuring distance of 5m [40]

11.3.2 ANSYS simulation results overview

	Sample Number	85	79	71	83	82	95	92	77
Imput values	Thermal Emittance εth [%]	0.85	0.85	0.83	0.85	0.85	0.85	0.84	0.83
	Solar Absorptance αsol [%]	0.97	0.97	0.97	0.97	0.97	0.97	0.97	0.97
	Temperature Thermocouple [°C]	624.3	710.6	713	630.8	713.2	713.2	593.3	667.5
	Distance Thermocouple from Skin [mm]	1.65	2	1.9	1.15	1.2	1.25	1.85	1.4
	Solar Flux Qsol [W/m2]	300.4	216.3	148.8	314.62	342.9	299.4	395.3	410.8
Iterated	h Value [W/m².°C]	528.8	399.6	400.5	528	407.25	407.25	607.5	467.6
Output values	Tskin, max [°C]	662.06	748.77	750.22	662.55	743.08	743.08	636.92	701.09
	Tinterface [°C]	644	731.8	733.19	644.5	726.03	726.03	618.59	683.44
	Tinside surface [°C]	581.62	677.6	678.81	582.16	671.26	671.26	545.27	624.59
	ΔT: Skin↔Thermocouple [°C]	37.76	38.17	37.22	31.75	29.88	29.88	43.62	33.59
	ΔT: Skin↔Interface [°C]	18.06	16.97	17.03	18.05	17.05	17.05	18.33	17.65
	ΔT: Skin↔Inside Surface [°C]	80.44	71.17	71.41	80.39	71.82	71.82	91.65	76.5

	Sample Number	76	70	89	88	84	78	73
Imput values	Thermal Emittance εth [%]	0.85	0.83	0.84	0.84	0.53	0.61	0.62
	Solar Absorptance αsol [%]	0.98	0.97	0.97	0.97	0.85	0.90	0.91
	Temperature Thermocouple [°C]	713	615.6	713.4	695.1	698.5	-	711.7
	Distance Thermocouple from Skin [mm]	1.8	2.1	1.65	1.5	1.45	1.85	1.2
	Solar Flux Qsol [W/m2]	358.4	364.9	333.6	153.4	311.6	340.6	226.3
Iterated	h Value [W/m².°C]	399.4	536	416	443.7	460.7	-	438.7
Output values	Tskin, max [°C]	749.02	659.09	749	729.84	715.08	-	724.93
	Tinterface [°C]	732.06	640.94	732.02	712.59	714.88	-	724.73
	Tinside surface [°C]	677.87	578.07	673.32	651.52	654.87	-	666.59
	ΔT: Skin↔Thermocouple [°C]	36.02	43.49	35.6	34.74	16.58	-	13.23
	ΔT: Skin↔Interface [°C]	16.96	18.15	16.98	17.25	-	-	-
	ΔT: Skin↔Inside Surface [°C]	71.15	81.02	75.68	78.32	60.21	-	58.34

11.3.3 Results of surface temperature measurement with IR camera

Sample Number	Raw value of measured Temperature (ε_{IR} = 1) [°C]	Emittance ε_{IR}	Weighted Temperature [°C]	ΔT [°C]	Average value for sample group [°C]
85	628.4	0.901	666.5	38.1	
79	735.6	0.903	780.9	45.3	
71	715.5	0.883	769.3	53.8	
83	645.3	0.895	687.2	41.9	
82	720.2	0.899	766.3	46.1	
95	721.8	0.904	765.5	43.7	45.8
92	615.8	0.895	655.3	39.6	
77	695.2	0.887	745.1	49.9	
76	729.0	0.897	776.8	47.8	
70	646.0	0.882	693.7	47.8	
89	726.4	0.897	774.1	47.6	
88	715.3	0.895	763.0	47.7	
84	489.0	0.693	596.4	107.4	
78	550.3	0.711	664.9	114.7	113
73	523.3	0.693	640.2	116.8	

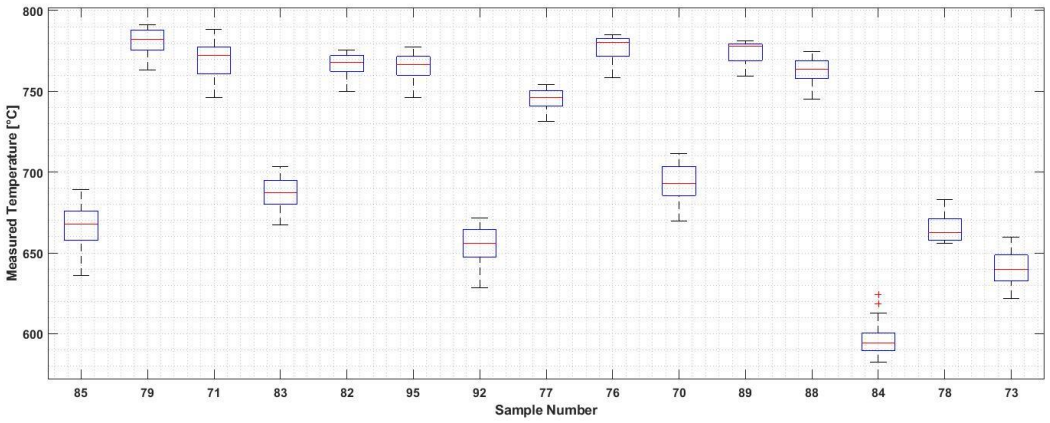

Figure 60: Boxplot of TMS 2 results (after emittance correction)

11.3.4 Comparison of different approaches for TMS1

Sample Number	$\Delta T_{Tool,flat}$ [°C]	$\Delta T_{Tool,tubular}$ [°C]	ΔT_{ANSYS} [°C]
85	27.2	23.3	37.8
79	28.8	24.1	38.2
71	28.2	23.8	37.2
83	24.7	22.0	31.8
82	24.9	22.1	29.9
95	25.5	22.4	31.3
92	28.7	24.1	43.6
77	26.1	22.7	33.6
76	28.0	23.7	36.0
70	29.3	24.4	43.5
89	27.6	23.5	35.6
88	26.8	23.1	34.7
84	6.5	3.3	16.6
78	8.7	4.5	20.2
73	5.7	2.9	13.2